J. Fluid Mech. (1995), *vol.* 299, *pp.* 35–71
Copyright © 1995 Cambridge University Press

A numerical study of flow past a rotating circular cylinder using a hybrid vortex scheme

By Y. T. CHEW, M. CHENG AND S. C. LUO
Department of Mechanical and Production Engineering, National University of Singapore, Singapore 0511

(Received 20 April 1994 and in revised form 24 April 1995)

The vortex shedding and wake development of a two-dimensional viscous incompressible flow generated by a circular cylinder which begins its rotation and translation impulsively in a stationary fluid is investigated by a hybrid vortex scheme at a Reynolds number of 1000. The rotational to translational speed ratio α varies from 0 to 6. The method used to calculate the flow can be considered as a combination of the diffusion-vortex method and the vortex-in-cell method. More specifically, the full flow field is divided into two regions: near the body surface the diffusion-vortex method is used to solve the Navier–Stokes equations, while the vortex-in-cell method is used in the exterior inviscid domain. Being more efficient, the present computation scheme is capable of extending the computation to a much larger dimensionless time than those reported in the literature.

The time-dependent pressure, shear stress and velocity distributions, the Strouhal number of vortex shedding as well as the mean lift, drag, moment and power coefficients are determined together with the streamline and vorticity flow patterns. When comparison is possible, the present computations are found to compare favourably with published experimental and numerical results. The present results seem to indicate the existence of a critical α value of about 2 when a closed streamline circulating around the cylinder begins to appear. Below this critical α, Kármán vortex shedding exists, separation points can be found, the mean lift and drag coefficients and Strouhal number increase almost linearly with α. Above $\alpha \approx 2$, the region enclosed by the dividing closed streamline grows in size, Kármán vortex shedding ceases, the flow structure, pressure and shear stress distributions around the cylinder tend towards self-similarity with increase α, and lift and drag coefficients approach asymptotic values. The optimum lift to drag ratio occurs at $\alpha \approx 2$. The present investigation confirms Prandtl's postulation of the presence of limiting lift force at high α, and thus the usefulness of the Magnus effect in lift generation is limited.

The results show that the present method can be used to calculate not only the global characteristics of the separated flow, but also the precise evolution with time of the fine structure of the flow field.

1. Introduction

The flow associated with a circular cylinder which begins its rotational and translational motion impulsively in a stationary fluid is a rather complex one. It includes the unsteady boundary layer separation flows which interact with the thin shear layers and wake flow, and generate complex unsteady lift and drag forces. When the ratio α of the rotational to translational speed is moderately high, a Kármán vortex street, Görtler-type vortices and Taylor vortices are generated at the same time (Matsui

1982). In particular, when the ratio is greater than a certain limiting value, Coutanceau & Ménard (1985) found that Kármán vortex street disappeared entirely during the early stage of their experiment. The fact that the unsteady features of the wake flow are still not fully understood has attracted both experimental and theoretical interest for a long time because of the considerable practical application of controlling moving-surface boundary layer separation to increase lift and reduce drag at high Reynolds numbers (Prandtl 1925; Prandtl & Tietjens 1934; Swanson 1961; Schlichting 1968; Tennant 1976). Moving all or part of a body surface also has applications in active or feedback control of vortex shedding, with important consequences for wake modification and the reduction of flow-induced vibration in offshore engineering (Gad-el-Hak & Bushnell 1991; Modi, Dobric & Yokomiz 1993; Chen, Ou & Pearlstein 1993).

Several experimental and numerical studies on flow past a rotating cylinder have already been conducted. The earliest visual experiments of flow past a rotating cylinder were carried out by Prandtl (1925). He argued that the maximum lift coefficient which could be realized by rotating the cylinder in free stream flow is 4π. Similar work was carried out later by Prandtl & Tietjens (1934). The experimental investigation of the complex flow field, especially the pressure distribution around the cylinder, is difficult to carry out because of the cylinder's rotation and the limitation of experimental equipment. Swanson (1961) overcame the difficulties of pressure measurements around the rotating cylinder by measuring the lift and drag forces directly. He found that there is a pronounced Reynolds number dependence of lift and drag forces in the region where the velocity ratio α is smaller than 1. Ludwig (1964) measured the velocity profiles of steady separation on a rotating cylinder for various low α in the range $\alpha \leqslant 0.3$. A criterion for laminar separation on a wall, which is applicable when the wall is either stationary or moving upstream or downstream, can be formulated from the experimental data. This criterion is defined and adopted in §4.3. Ludwig found that the position of laminar separation on the downstream-moving wall of the cylinder is linearly dependent on the velocity ratio α. Peller (1986) investigated the steady separation on a heated and rotating cylinder in cross-flow at subcritical Reynolds number. His measured two-dimensional boundary layer profiles are similar to those obtained by Ludwig (1964). Chew (1987) measured the pressure distributions around a rotating cylinder directly by using a single pressure transducer with mercury slip ring and the ensemble-averaging technique. The results clearly indicate the shift in mean separation locations in the direction of rotation, the shift in stagnation location against the direction of rotation, and the asymmetry of mean pressure distribution around the cylinder which results in increasing lift force with increasing α. Recently, a method for estimating the mean lift of a rotating cylinder in uniform flow was presented by Tokumaru & Dimotakis (1993) for Reynolds numbers $Re = 3.8 \times 10^3$. Their determination of the mean lift is based on an inviscid point-vortex model and the transverse velocity measured experimentally ahead of the cylinder. Their results showed that large α yields higher lift coefficients for a cylinder rotating at constant speed. They reported that when $\alpha < 1$, the lift coefficients they estimated are higher than the results of Reid (1924). At larger values of $\alpha > 5$, the maximum lift coefficients exceed 4π (the limiting magnitude suggested by Prandtl 1925) by more than 20%. Tokumaru & Dimotakis' results also show that although the lift coefficient increases with α, the rate of increase becomes gradually smaller as α exceeds 4.

In view of the experimental difficulties, the solutions of the Navier–Stokes equations using analytical and computational methods provide an excellent alternative description of the viscous fluid motions. The earlier analytical studies concerning steady flow were carried out by Wood (1957), Moore (1957) and Glauert (1957). Their studies indicated that, for sufficiently high α, it is possible to use the method of matched expansions to obtain steady flows without vortex shedding at both high and low Reynolds numbers *Re* (based on the cylinder diameter and the magnitude of the velocity at infinity). More recently, using a power series method, the steady-state limit of the solution of the time-dependent Navier–Stokes equations together with a verification obtained from the steady-state equation was obtained by Badr, Dennis & Young (1989) for low Reynolds numbers and small α. They found that when the cylinder starts moving impulsively from rest, the flow approaches a steady state after a sufficiently long time for the low Reynolds numbers situation, but at a higher Reynolds number of 60, the flow does not tend to a steady state but instead develops a periodic pattern of vortex shedding. However, Tang & Ingham (1991) extended the Reynolds number range up to 100, but did not observe the periodic pattern of vortex shedding. On the other hand, using both Fourier analysis and experimental flow visualization, the unsteady flow past a circular cylinder which begins translational and rotational motion impulsively from rest in a viscous fluid was investigated by Badr & Dennis (1985) and Badr *et al.* (1990) for $Re = 200$, 500 and $10^3 \leqslant Re \leqslant 10^4$ and for α in the range of 0.5 to 3. With the exception of the case with the highest α ($= 3$), the flow structure estimated by numerical calculation was found to be in excellent agreement with the experimental results. When $\alpha = 3$ and at dimensionless time $t > 10$, they found that the three-dimensional effects become more pronounced in the experiments and the laminar flow breaks down, while the calculated flow starts to approach a steady state. For the quite wide range of *Re* from 10^3 to 10^6 and the α range of 0 to 2, the initial stage of the flow past a rotating circular cylinder has been studied by Chang & Chern (1991*b*) using a hybrid vortex method which consists of solving the Poisson's equation for the stream function and the viscous vorticity transport equation by interlacing a finite-difference method for viscous diffusion and a vortex-in-cell algorithm for convection.

However, the common points of interest of these unsteady flow investigations are the initial structure of vortex formation and shedding in the near-wake flow within a certain Reynolds number and α range. The numerical studies are mostly limited to flows over a short time and so cannot investigate fully the complete structure of flow field as well as the global characteristics of the wake in a fully developed flow. At low Reynolds number, the development of the wake behind a circular cylinder impulsively started into rotational and translational motion has been studied computationally by Chen *et al.* (1993) over a longer period of time. Their results indicate that at $Re = 200$, shedding of more than one vortex still occurs at $\alpha = 3.25$, which is contrary to the finding of Coutanceau & Ménard (1985).

The present paper presents results for vortex shedding and the full development of the wake behind a rotating cylinder at higher Reynolds number and over a much wider range of α. It is well known that for high Reynolds number flow past a circular cylinder, the effects of viscosity are generally limited to the thin boundary layers on the cylinder and wake behind it. Thus, the distribution of vorticity in the field is sufficiently compact for its idealization in terms of singularities embedded in an otherwise inviscid domain. The higher the Reynolds number, the more compact are the regions of vorticity, so that the real flow can be simulated by a discrete vortex blob distributed in the flow field. The discrete-vortex method is capable of predicting effectively the global features of unsteady separated flow and the flow field far from the cylinder. An excellent review on this method has been written by Sarpkaya (1989). Other researchers (Kimura & Tsutahara 1987; Cheng, Ling & Zhuang 1990; Chew, Cheng & Luo 1993) have studied the flow past a rotating circular cylinder using the discrete-vortex model combined with boundary layer theory and the diffusion-vortex model for a small rotational parameter. The results showed that the vortex method is both simple and efficient for predicting lift and drag forces that are consistent with the experimental results reported by Swanson (1961) and Ludwig (1964). Similarly, in the present paper, the vortex shedding and wake development is simulated by a hybrid vortex scheme: a combination of the diffusion-vortex method proposed by Lu & Ross (1991) and the vortex-in-cell method developed by Christiansen (1973). More specifically, the full flow field is divided into two regions. In the region near the body surface the diffusion-vortex method is used to solve the Navier–Stokes equations, while the vortex-in-cell method is used in the exterior domain. Being more efficient, the present computation scheme can extend the computation to a much larger dimensionless time than those schemes used by other researchers (Badr *et al.* 1990; Chang & Chern 1991*b*; Chen *et al.* 1993). The present calculation will throw some light on the unsteady separation, the development of a periodic pattern of vortex shedding associated with the Kármán vortex street behind a rotating cylinder at high Reynolds number, the relation between the Strouhal number of vortex shedding and rotational parameter α, the pressure distributions around the rotating cylinder as well as the forces acting on it at different values of the rotational parameter.

2. Physical equations and boundary conditions

In the present analysis the flow is assumed to be two-dimensional, viscous and incompressible. The origin of the frame of reference $(\tilde r, \theta)$ coincides with the centre of the cylinder which rotates about its axis in the counterclockwise direction with a constant angular velocity $\tilde\omega$, as shown in figure 20. The directions of positive $\tilde U_\infty, \tilde\omega, \tilde r$ and θ are also as shown.

The flow is governed by the continuity and Navier–Stokes equations. They can be written as

$$\nabla\cdot\tilde{\boldsymbol{u}} = 0, \tag{1}$$

$$\frac{\partial\tilde{\boldsymbol{u}}}{\partial\tilde t}+(\tilde{\boldsymbol{u}}\cdot\nabla)\,\tilde{\boldsymbol{u}} = -\frac{1}{\tilde\rho}\nabla\tilde p+\tilde\nu\nabla^2\tilde{\boldsymbol{u}}. \tag{2}$$

The stream function $(\tilde\psi)$ and vorticity $(\tilde\zeta)$ can be obtained from (1) and (2):

$$\frac{\partial\tilde\zeta}{\partial\tilde t}+\frac{1}{\tilde r}\left(\frac{\partial}{\partial\tilde r}\left(\tilde\zeta\frac{\partial\tilde\psi}{\partial\theta}\right)-\frac{\partial}{\partial\theta}\left(\tilde\zeta\frac{\partial\tilde\psi}{\partial\tilde r}\right)\right) = \tilde\nu\nabla^2\tilde\zeta, \tag{3}$$

$$\nabla^2\tilde\psi = -\tilde\zeta. \tag{4}$$

The relations of stream function and vorticity with velocity $\tilde{\boldsymbol{u}}$ are

$$\tilde{\boldsymbol{u}} = \nabla\times(\tilde\psi\boldsymbol{k}), \tag{5}$$

$$\tilde\zeta\boldsymbol{k} = \nabla\times\tilde{\boldsymbol{u}}. \tag{6}$$

Dimensionless variables are defined according to

$$r=\frac{\tilde r}{\tilde a},\quad \boldsymbol{u}=\frac{\tilde{\boldsymbol{u}}}{\tilde U_\infty},\quad \psi=\frac{\tilde\psi}{\tilde U_\infty\tilde a},\quad \zeta=\frac{\tilde a\tilde\zeta}{\tilde U_\infty},\quad t=\frac{\tilde U_\infty\tilde t}{\tilde a},\quad \alpha=\frac{\tilde a\tilde\omega}{\tilde U_\infty},\quad Re=\frac{2\tilde a\tilde U_\infty}{\tilde\nu}, \tag{7}$$

where the tilde denotes the dimensional variables, $\tilde r$ and θ are the usual cylindrical polar coordinates, $\tilde\nu$ is the kinematic viscosity, $\tilde t$ is the time, $\boldsymbol{k}$ is a unit vector in the direction of the cylinder axis, $\tilde U_\infty$ is the velocity at infinity, and $\tilde a$ is the radius of the cylinder.

In order to emphasize the region near the wall $r = 1$, it is convenient to introduce the transformation

$$\xi = \ln r, \tag{8}$$

and equations (3) and (4) can then be written in dimensionless form as

$$\frac{\partial \zeta}{\partial t} - e^{-2\xi}\frac{\partial(\psi, \zeta)}{\partial(\xi, \theta)} = \frac{2}{Re} e^{-2\xi} \nabla^2 \zeta, \tag{9}$$

$$\nabla^2 \psi = -e^{2\xi} \zeta. \tag{10}$$

The boundary conditions for $t \geqslant 0$ for equations (9) and (10) are

$$\psi|_{\xi=0} = 0, \tag{11}$$

$$(\partial \psi / \partial \xi)|_{\xi=0} = \alpha, \tag{12}$$

$$\left(e^{-\xi} \frac{\partial \psi}{\partial \xi} \right) \Bigg|_{\xi \to \infty} \to \sin \theta, \tag{13}$$

$$\psi|_{\theta=0} = \psi|_{\theta=2\pi}, \tag{14}$$

$$\zeta|_{\xi=0} = \zeta(t, \theta) \tag{15}$$

to be given, and

$$\zeta|_{\theta=0} = \zeta|_{\theta=2\pi}. \tag{16}$$

3. Calculation method

3.1. *The hybrid vortex algorithm*

It is well known that the vorticity transport equation (9) represents the two mechanisms of vorticity diffusion and vorticity convection which occur simultaneously. For high Reynolds number flow, following Chorin (1973), the time integration may be broken into two fractional steps: pure diffusion and inviscid convection, in order to simplify the problem. Thus, during time step Δt, the pure linear diffusion equation

$$\frac{\partial \zeta}{\partial t} = \frac{2}{Re} e^{-2\xi} \nabla^2 \zeta, \tag{17}$$

and the inviscid convection equation

$$\frac{\partial \zeta}{\partial t} - e^{-2\xi}\frac{\partial(\psi, \zeta)}{\partial(\xi, \theta)} = 0 \tag{18}$$

are solved separately.

In order to effectively solve (17) and (18) by applying the hybrid vortex scheme, the full flow field is covered by a net of mesh points, and is divided into two regions. Region 1 ($0 \leqslant \xi < \xi_1$) is the layer with thickness of $O(\delta)$ near the cylinder surface, where δ is the boundary layer thickness on the surface of the cylinder. The thickness of region 1 is estimated from the flat-plate boundary layer thickness (constant $(\pi/Re)^{1/2}$, Schlichting 1968). Region 2 ($\xi_1 \leqslant \xi \leqslant \xi_\infty$) is the slightly viscous flow region outside the region 1 extending to infinity.

In region 1, the flow is viscous, the vorticity produced at the wall is carried away by convection and diffusion, flow separation occurs and there is large deformation of streamlines. These processes determine the entire flow field which in turn controls the production of vorticity. The diffusion-vortex method is used to simulate the unsteady flow field near the wall, since it not only avoids the difficulties in cut-off properties of the vortices but also reduces the CPU time required (Lu & Ross 1991).

When the vorticity distribution at time t_0 is known, the vorticity field ζ at $t_0 + \Delta t$ can be determined by applying the diffusion-vortex method. In other words, each vortex diffuses during Δt to spread its vorticity in a Gaussian distribution to all the mesh points. By summing all contributions, new vortices are created at the mesh points after each time step Δt. They are then convected according to equation (18). The detailed process will be given later. The redistribution of vorticity to the mesh points at each time step can cause numerical diffusion. However, when mesh length $h (h = \max(\Delta r, r\Delta\theta))$ satisfies the condition $h \leqslant 1.756(\Delta t/Re)^{1/2}$ which is maintained in the present computation, the error generated by the vorticity redistribution is of $O(10^{-5})$. The detailed proof is given by Lu & Ross (1991).

In region 2, the effects of viscosity can be neglected for high Reynolds number. Therefore, the flow far away from the cylinder can be approximated as inviscid potential flow and can undergo only convection and deformation according to equation (18). This will be examined further in §4. The convection of a vortex is calculated using the vortex-in-cell method. Namely, when a vortex with a certain strength reaches its new location, it contributes incremental vorticity to the four surrounding mesh points according to the area-weighting scheme. In contrast to the usual Lagrangian vortex methods, these vortices move only one time step. This process of vorticity redistribution introduces a pseudo-viscosity into the flow, but it may be regarded as an advantage for it stabilizes the velocity field calculation (Sarpkaya 1989). The numerical diffusion is more significant in the far wake, but the influence on the vortex shedding frequency, lift and drag force is small when fine meshes are used in the computation.

The velocity of the convection motion is determined via the stream function by solving the Poisson equation (10) together with the boundary conditions (11), (13) and (14). After vorticity is redistributed to replace the initial vorticity field, the calculation procedure is repeated until the end of the time period of interest.

3.2. *Initial vorticity condition*

Since the diffusion equation is being solved in region 1, it is necessary to know the initial vorticity distribution. The vorticity is initially confined to an infinitesimally thin region surrounding the cylinder surface. The asymptotic formula given by Badr & Dennis (1985) is taken as the initial distribution of vorticity:

$$\zeta|_{\xi=0} \approx \frac{1}{A}\left\{\alpha\left(\frac{2}{\pi^{1/2}}-\frac{A}{2}\right)+\left(\frac{4}{\pi^{1/2}}+A\right)\sin\theta+\left(2.7844A-\frac{16}{3\pi^{3/2}}\right)\alpha t\cos\theta\right.$$
$$\left.+\left[6.5577A-\frac{4}{\pi^{1/2}}\left(1+\frac{4}{3\pi}\right)\right]t\sin 2\theta\right\}, \quad (19)$$

and
$$\zeta|_{\xi>0} = 0, \quad (20)$$

where
$$A = (8t/Re)^{1/2}. \quad (21)$$

3.3. *The vorticity distribution after a lapse of time*

In region 1 near the surface of the cylinder, the vorticity distribution is determined by equation (17). Let us consider the vorticity diffusion equation, with the initial distribution $\zeta_0(r, \theta, t_0)$ at time t_0 and given $\zeta_B(t)$ along the boundary:

$$\frac{\partial\zeta}{\partial t} = \frac{2}{Re}\mathrm{e}^{-2\xi}\nabla^2\zeta, \quad (22)$$

$$\zeta|_B = \zeta_B, \quad (23)$$

$$\zeta|_{t=t_0} = \zeta_0. \quad (24)$$

The solution of (22), (23) and (24) at time $t_0 + \Delta t$ can be written as (Barton 1989)

$$\zeta(r, \theta, t_0 + \Delta t) = \iint_S G\zeta_0(r', \theta', t_0)\, r'\, \mathrm{d}r'\, \mathrm{d}\theta' - \frac{2}{Re}\int_{t_0}^{t_0+\Delta t} \mathrm{d}\tau \int_L \zeta_B \left.\frac{\partial G}{\partial n}\right|_B dL, \qquad (25)$$

where G is the appropriate Green's function, defined by

$$\frac{\partial G}{\partial t} = \frac{2}{Re}\nabla^2 G + \delta(r - r')\,\delta(\theta - \theta')\,\delta(t - \tau), \qquad (26)$$

$$G|_B = 0 \quad (t > \tau) \qquad (27)$$

and $\partial G/\partial n|_B$ indicates the derivative in the direction normal to the surface B.

For high Reynolds number flow, one can use the flat-plate solution as an approximation to the solution when the wall boundary is divided into very short segments. Therefore, the diffusion process of a continuous vorticity field in region 1 can be written as

$$\zeta(\xi, \theta, t_0 + \Delta t) = \iint_S \zeta_0(\xi', \theta', t_0)\, G\, \mathrm{d}S - \frac{2}{Re}\int_{t_0}^{t_0+\Delta t} \mathrm{d}\tau \int_L \zeta_B \left.\frac{\partial G}{\partial n}\right|_B \mathrm{d}L, \qquad (28)$$

where

$$G = \frac{1}{4\pi\,\Delta t\gamma^2}\left(e^{-r_1^2/(4\Delta t\gamma^2)} - e^{-r_2^2/(4\Delta t\gamma^2)}\right), \qquad (29)$$

$$\left.\frac{\partial G}{\partial n}\right|_B = \frac{4}{(4\Delta t\gamma^2)^2\pi}[1 - e^{\xi}\cos(\theta - \theta')]\exp\left(-\frac{1 + e^{2\xi} - 2e^{\xi}\cos(\theta - \theta')}{4\Delta t\gamma^2}\right), \qquad (30)$$

$$r_1^2 = e^{2\xi} + e^{2\xi'} - e^{\xi+\xi'}\cos(\theta - \theta'), \qquad (31)$$

$$r_2^2 = e^{2\xi} + e^{-2\xi'} - e^{\xi-\xi'}\cos(\theta - \theta'), \qquad (32)$$

$$\gamma^2 = 2/Re. \qquad (33)$$

The flow in region 2 is approximated as inviscid potential flow. The vorticity is conserved when the vortex is in motion. The distribution of vorticity can be calculated using the vortex-in-cell method: when a vortex with strength Γ reaches its new location, it contributes incremental vorticity ζ to the four surrounding mesh points according to the area-weighting scheme. The corresponding vorticity distribution on grid nodes is

$$\zeta_i = \frac{A_i}{A^2}\Gamma \quad (i = 1, 2, 3, 4), \qquad (34)$$

where A is the grid cell area and A_i is the area opposite the ith node.

3.4. *Convection simulation*

After the vorticity distribution at each mesh point (ξ_i, θ_i) at time t is calculated, the velocity is determined via the stream function by solving the Poisson equation (10) together with the boundary conditions (11), (13) and (14). Here (10) will be solved by a subroutine (FPS2H), available from the IMSL mathematical package, for solving Poisson equations. The subroutine is based on representing the elliptic equation in finite-difference form using a method developed by Lynch & Rice (1978) and known as the HODIE (high order difference approximation with identity expansion) method. The resulting system of linear algebraic equations is solved using fast-Fourier-transform techniques (Boisvert 1984). The stream function ψ is related to the velocity components through

$$v_r = \mathrm{e}^{-\xi}\partial\psi/\partial\theta, \tag{35}$$

$$v_\theta = -\mathrm{e}^{-\xi}\partial\psi/\partial\xi. \tag{36}$$

According to equation (18), the vortex at each mesh point is displaced after a time interval Δt to the location

$$r(t+\Delta t) = r(t)+\tfrac{1}{2}[3v_r(t+\Delta t)-v_r(t)]\,\Delta t, \tag{37}$$

$$\theta(t+\Delta t) = \theta(t)+\frac{1}{2r(t)}[3v_\theta(t+\Delta t)-v_\theta(t)]\,\Delta t. \tag{38}$$

3.5. *Vorticity distribution on the cylinder surface for the next time step*

The vorticity boundary condition is determined from the Poisson equation (10), and a second-order formula is proposed:

$$\zeta|_{\xi=0} = -\frac{6[\psi(\Delta\xi,\theta,t)+\alpha\Delta\xi]+\zeta(\Delta\xi,\theta,t)\,\Delta^2\xi}{2\Delta^2\xi}. \tag{39}$$

3.6. *Calculation of force coefficients*

The lift, drag, moment and power coefficients are defined according to

$$C_L = \frac{\tilde{L}}{\tilde{\rho}\tilde{U}_\infty^2\,\tilde{a}}, \quad C_D = \frac{\tilde{D}}{\tilde{\rho}\tilde{U}_\infty^2\,\tilde{a}}, \quad C_M = \frac{\tilde{M}}{\tilde{\rho}\tilde{U}_\infty^2\,\tilde{a}^2}, \quad C_N = \frac{\tilde{N}}{\tilde{\rho}\tilde{U}_\infty^3\,\tilde{a}}, \tag{40}$$

where $\tilde{L}$, $\tilde{D}$ and $\tilde{M}$ are the lift, drag and moment exerted by the fluid on unit length of the rotating cylinder, $\tilde{N}$ is the power needed to maintain the rotation of the cylinder, and $\tilde{\rho}$ is the fluid density.

The velocity and vorticity at time t obtained by the computation can be used to calculate the pressure and shear stress distributions on the surface of the cylinder, namely

$$C_p = \frac{\tilde{p}-\tilde{p}_\infty}{\frac{1}{2}\tilde{\rho}\tilde{U}_\infty^2} = 1-\alpha^2+2\int_1^\infty\left(\frac{2}{Re}\frac{1}{r}\frac{\partial\zeta}{\partial\theta}+\frac{\partial v_r}{\partial t}-v_\theta\zeta\right)\mathrm{d}r, \tag{41}$$

$$C_\sigma = \frac{\tilde{\sigma}_{r\theta}}{\frac{1}{2}\tilde{\rho}\tilde{U}_\infty^2} = \frac{4}{Re}\left[r\frac{\partial}{\partial r}\left(\frac{v_\theta}{r}\right)\right]_{r=1}, \tag{42}$$

where $\tilde{p}_\infty$ is the static pressure at infinity.

The pressure and the shear stress components of the drag and lift coefficients are obtained from the following integration:

$$C_{Dp} = -\frac{1}{2}\int_0^{2\pi} C_p\cos\theta\,\mathrm{d}\theta, \qquad C_{Lp} = -\frac{1}{2}\int_0^{2\pi} C_p\sin\theta\,\mathrm{d}\theta, \tag{43a,b}$$

$$C_{D\sigma} = -\frac{1}{2}\int_0^{2\pi} C_\sigma\sin\theta\,\mathrm{d}\theta, \qquad C_{L\sigma} = \frac{1}{2}\int_0^{2\pi} C_\sigma\cos\theta\,\mathrm{d}\theta. \tag{44a,b}$$

The total drag and lift coefficients are given by

$$C_D = C_{Dp}+C_{D\sigma}, \quad C_L = C_{Lp}+C_{L\sigma}. \tag{45a,b}$$

The moment and power coefficient are similarly obtained from the following integration:

$$C_M = -\frac{1}{2}\int_0^{2\pi} C_\sigma \, \mathrm{d}\theta, \qquad C_N = -\frac{1}{2}\int_0^{2\pi} \alpha C_\sigma \, \mathrm{d}\theta. \qquad (46a, b)$$

4. Results and discussion

The numerical calculation of the flow past a rotating circular cylinder is carried out for $Re = 1000$ and the rotational to translational speed ratio α in the range $0 \leqslant \alpha \leqslant 6$ on an IBM 3090 mainframe computer. The total computation domain has been limited to $\xi_\infty = 3\pi/2$. In the present calculation region 1 corresponds to $0 \leqslant \xi \leqslant 0.4$ and region 2 to $0.4 \leqslant \xi \leqslant \xi_\infty$. The influence of the number of grid points and the size of region 1 have been checked for the lift and drag coefficients. It is found that the lift and drag coefficients decrease with increasing size of region 1, but the change is very small. When region 1 increases from $0 \leqslant \xi \leqslant 0.2$ to $0 \leqslant \xi \leqslant 0.8$, the mean values of lift and drag coefficients decrease by about 5%. However, the lift and drag coefficients increase with increasing the number of grid points. When the nodes increase from $I \times J = 129 \times 257$ to 257×513 (where I and J are the number of basic grid points in the ξ- and θ-directions respectively), the lift and drag coefficients increase by about 6% and 8%, respectively. When the nodes increases from $I \times J = 257 \times 513$ to 513×513, the lift and drag coefficients only increase by less than 2%. It is found that a grid system of $I \times J = 257 \times 513$ nodes is sufficient and is adopted for all subsequent computation. The calculation for this problem starts at $t_0 = 0.001$, using the asymptotic formula given by Badr & Dennis (1985) (equations (19)–(21)). In the calculation, the vorticity on the cylinder is sensitive to the grid size at rotational parameter $\alpha > 1$. Since the diffusion and convection are calculated separately in the present method, the vorticity transfer not only depends on the grid size but also on the size of the time step Δt. On the basis of convection stability considerations, the non-dimensional time step is chosen as $\Delta t = 0.02$ when $\alpha \leqslant 1$, and $\Delta t = 2.4\Delta\xi/\alpha$ when $\alpha > 1$. The CPU time required for each time step is about 2.8 s.

As a further simple check on the numerical scheme, during the calculation, it is found that the rate of change of the net sum of circulation on the cylinder surface remains approximately zero in finite time

$$\left(\sum_{j=1}^{J} \frac{\partial}{\partial t}(\Delta \Gamma_j)\,\Delta t = 0\right).$$

This is consistent with the surface condition presented by Stansby & Smith (1991).

4.1. *The vortex shedding and wake evolution*

The streamlines around the cylinder for $\alpha = 0$ at different times are shown in figures 1 and 2. A comparison with the results of Chang & Chern (1991*a*) for $Re = 1000$ from $t = 1$ to 6, is given in figure 1(*a*–*d*) in order to provide an independent verification of the present calculation method. In figure 1, since the flow is symmetrical about the line $\theta = 0°$, only one half of each flow will be shown. The values of streamlines plotted are -0.4, -0.2, -0.1, -0.05, -0.025, -0.012, 0.001, 0.008, 0.02, 0.04, 0.08, 0.15, 0.3, 0.65 and 1.3. Generally, agreement between the results obtained by the two methods is good. Both show the elongation with time of the main vortex and the appearance of a secondary vortex near the separation point at time $t = 3$. The secondary vortex grows

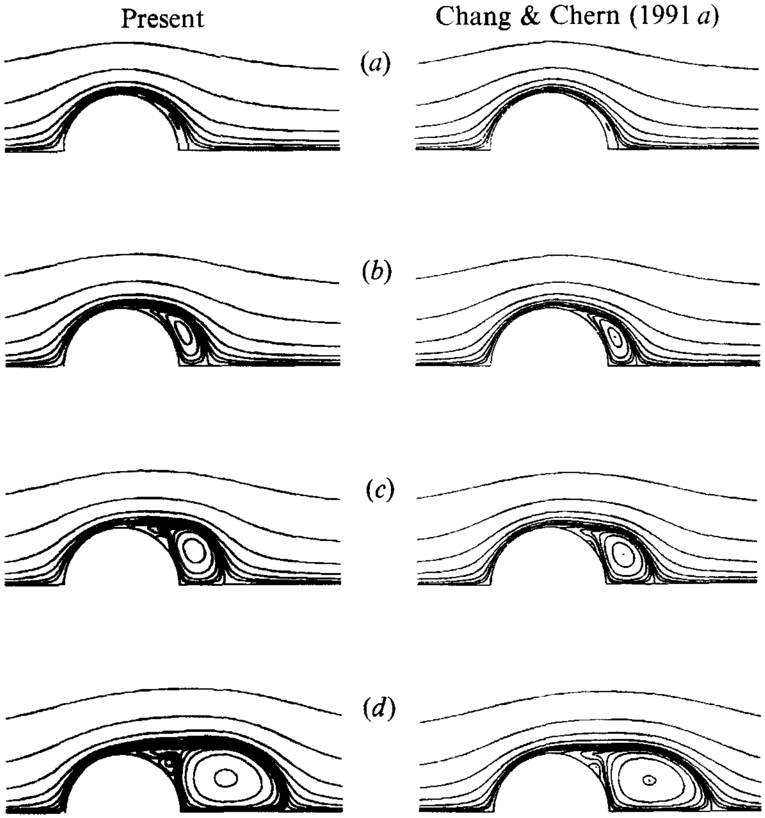

FIGURE 1. Comparison of the development of streamline patterns from two numerical methods for $Re = 1000$, $\alpha = 0$ at times (*a*) $t = 1$, (*b*) $t = 2$, (*c*) $t = 3$, (*d*) $t = 6$.

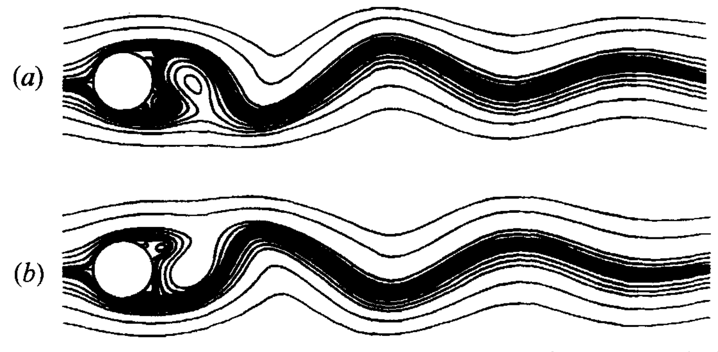

FIGURE 2. Patterns of instantaneous streamlines during half a cycle of vortex shedding for $\alpha = 0$. (*a*) $t = 55$, (*b*) $t = 60$.

in size until it touches the boundary of the main recirculation zone, and splits the main vortex into two parts. Two secondary vortices emerge near the separation location and constitute the so-called α-phenomenon at $t = 6$. One can find from figure 1 that the dimensionless wake lengths at $t = 1$, 2, 3 and 6 are 0.22, 0.5, 0.8 and 1.8 respectively, in good agreement with the results of Ta Phuoc Loc (1980). In addition, comparison of the time evolution of vorticity distribution over the surface of the cylinder with the analytic results of Bar-Lev & Yang (1975) and Collins & Dennis (1973) have been

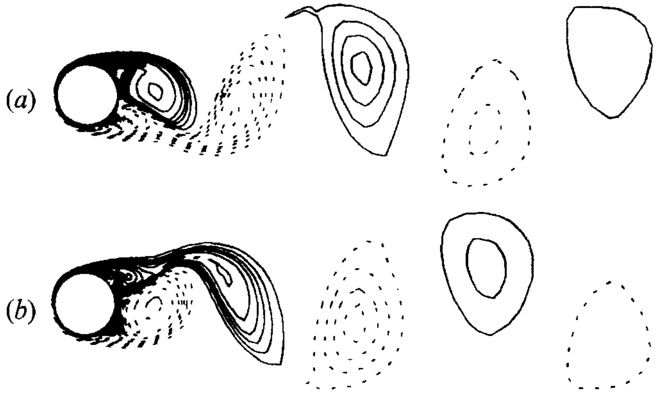

FIGURE 3. Vorticity contours at several time instants during half a cycle of vortex shedding for $\alpha = 0$. (*a*) $t = 55$, (*b*) $t = 60$. Dashed (solid) lines represent constant positive (negative) vorticity values, in this and subsequent figures.

carried out for $Re = 1000$. It is found that the present results are also in good agreement with their results for the early stages of the flow.

In numerical calculations of such a flow, there are no destabilizing effects except for the numerical errors. Since the geometry of the flow domain and the boundary conditions are symmetrical, the solution of the equations is also symmetrical. This happens in the present case. Therefore an initial perturbation to the wake is required in order to initiate the alternate vortex shedding. In the present study, a rotation of the cylinder is imposed for a short duration to provide the initial perturbation. After a period of evolution, a periodic wake called the von Kármán vortex street appears at $t > 25$ as shown in figure 2(*a*, *b*).

Figure 3 shows the vorticity contours at several time instants during half a cycle of vortex shedding. Whilst the vortex on one side is being shed, the one on the other side is reforming. It is well known that flow around a fixed circular cylinder may remain highly two-dimensional only up to a Reynolds number of 200 (Williamson 1989) owing to the perturbation in the real flow. At high Reynolds number, real flow will only remain two-dimensional in the starting flow for a limited time. In the present two-dimensional numerical simulation, some long time simulations are also conducted to obtain frequency information on vortex shedding. For example, when $\alpha = 0$ in figure 3, the alternating vortices with the same strength advance downstream and the dimensionless vortex shedding frequency f is equal to 0.103, where $f = 1/T$ and T is the dimensionless period of vortex shedding. The Strouhal number St is related to f by $St = 2f$, and at $Re = 1000$, St obtained by Roshko (1954) in his experiment is about 0.21 or $f = 0.105$.

The patterns of instantaneous streamlines for $\alpha = 0.5$ at different times are shown in figures 4 and 5. In figure 4, the present results are shown next to those of Badr *et al.* (1990) for $Re = 1000$. Figure 4(*a*) shows the existence of the first vortex and a bulging of streamlines near the right lower side of the cylinder at the beginning of impulsively started motion. The first vortex grows gradually in the upper wake while the bulge leads to the formation of the second vortex as shown in figure 4(*b*). At $t = 3$, a secondary vortex appears near the cylinder in the neighbourhood of the second vortex (figure 4*c*) and this secondary vortex is still present at $t = 4$ as shown in figure 4(*d*). It should be noted in figure 4 that the initial perturbation was not added artificially. The rotation creates asymmetry in the formation of wake flow behind the cylinder. The streamline patterns compare favourably with the results of Badr *et al.* (1990). After a (*a*) Present (*b*) Present

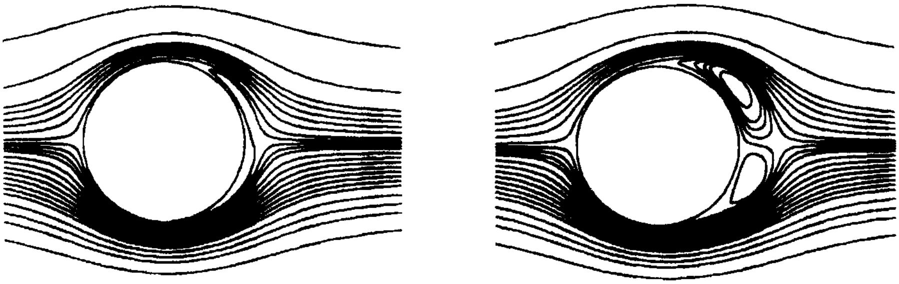

Badr *et al.* (1990) Badr *et al.* (1990)

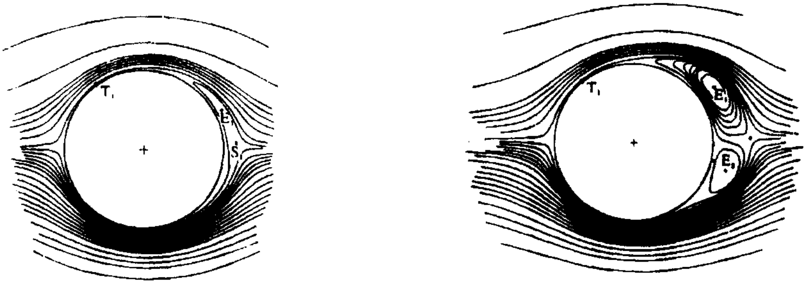

FIGURE 4(*a*,*b*). For caption see facing page.

longer time, alternating vortices are shed from the upper and lower sides of the cylinder as shown in figure 5. As the shed vortices steadily move away from the cylinder in the downstream direction, streamlines show a periodic fluctuation that looks like a travelling wave. One interesting feature that is found in the present results is that as time advances the secondary vortex still appears periodically as shown in figures 5(*a*) and 5(*c*). It appears as a small companion vortex to the main vortex at the lower side of the cylinder. Furthermore, the vortex structures formed on the upper side of the cylinder as shown in figures 5(*b*) and 5(*d*) are different from that formed on the lower side of the cylinder as observed in figures 5(*a*) and 5(*c*). This is because, owing to the anticlockwise rotation of the cylinder, vorticity of opposite sign is generated which diffuses into and weakens the secondary vortex on the upper side, and creates the companion secondary vortex on the lower side. The secondary vortices generated during the transient stage are of opposite vorticity to the main vortices, i.e. anticlockwise on the upper side and clockwise on the lower side. The relative velocity between the moving cylinder surface and the flow in these secondary vortices tends to decrease the strength of the secondary vortex on the upper side and increase it on the lower side. Figure 6 shows the vorticity contours at different time during two cycles of vortex shedding for $\alpha = 0.5$. When $t = 8$ (figure 6*a*), the first vortex (a negative or clockwise vortex) is shed from the upper side of the cylinder. The second vortex (a positive or anticlockwise vortex) is shed from the lower side of the cylinder at $t = 12$ (figure 6*b*). It takes about 19 dimensionless times for two cycles of vortex shedding to be completed. The mean value of the vortex shedding frequency estimated from 10 vortex shedding cycles is $f = 0.108$, and the corresponding Strouhal number is 0.216.

When $\alpha = 1$, the pattern of streamline evolution is found to be basically the same as for $\alpha = 0.5$. However, the positive vortex is formed in the $0° < \theta < 90°$ region and, when fully formed, is shed and then moves away from that region. A highly regular

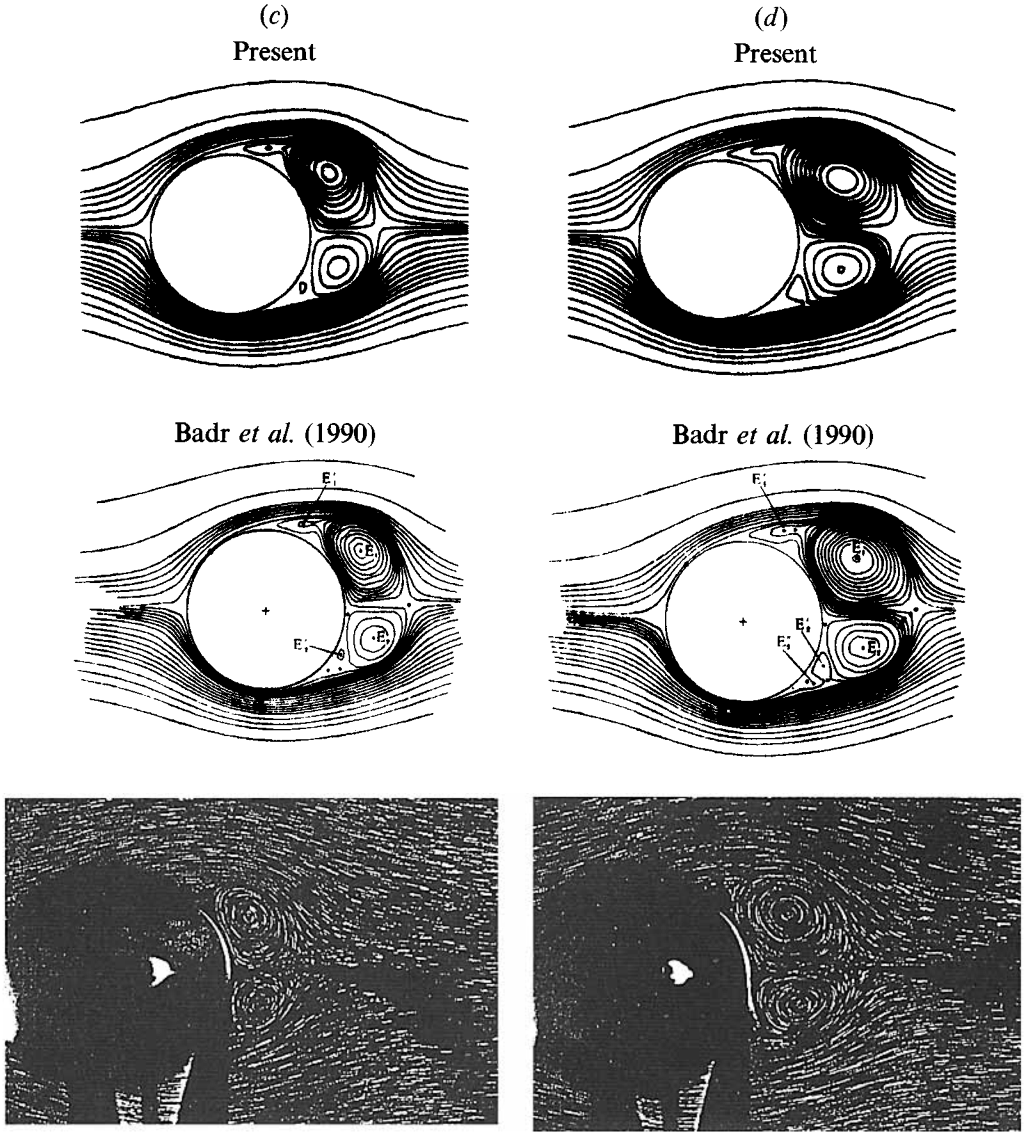

FIGURE 4. Comparison of the development of streamline patterns from two numerical methods and experimental flow visualization for $\alpha = 0.5$ at times (*a*) $t = 1$, (*b*) $t = 2$, (*c*) $t = 3$, (*d*) $t = 4$.

fluctuation is shown in figure 7. The companion secondary vortex associated with the main vortex on the lower side is also highly visible in figures 7(*a*) and 7(*c*), while none is found on the upper side. Figure 8 shows time sequences of vorticity contours covering two cycles of vortex sheddings for $\alpha = 1$: the first vortex is shed at $t = 7$ (figure 8*a*) and the third vortex is shed at $t = 16$ (figure 8*c*); the phenomenon is repeated about every 9 dimensionless time periods. The mean vortex shedding frequency estimated from 10 vortex shedding cycles is $f = 0.115$, and the corresponding Strouhal number is 0.23. Another interesting phenomenon that can be observed is that the vortices shed from the upper side are stronger than those from the lower side of the cylinder in starting flow only for a limited time. This phenomenon is also present in the results of Chen *et al.* (1993) at $Re = 200$. It should be noted in the present results that

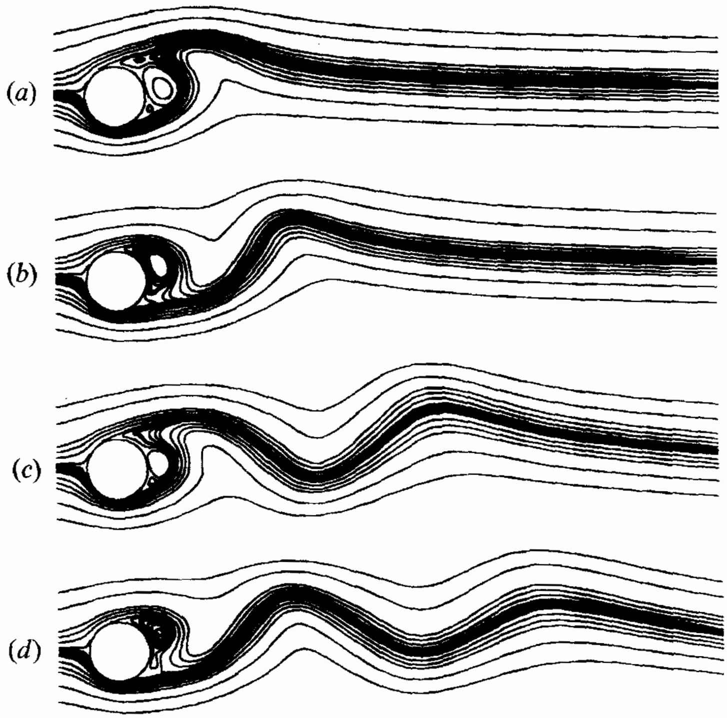

FIGURE 5. Patterns of instantaneous streamlines during two cycles of vortex shedding for $\alpha = 0.5$. (*a*) $t = 8$, (*b*) $t = 12$, (*c*) $t = 17$, (*d*) $t = 21$.

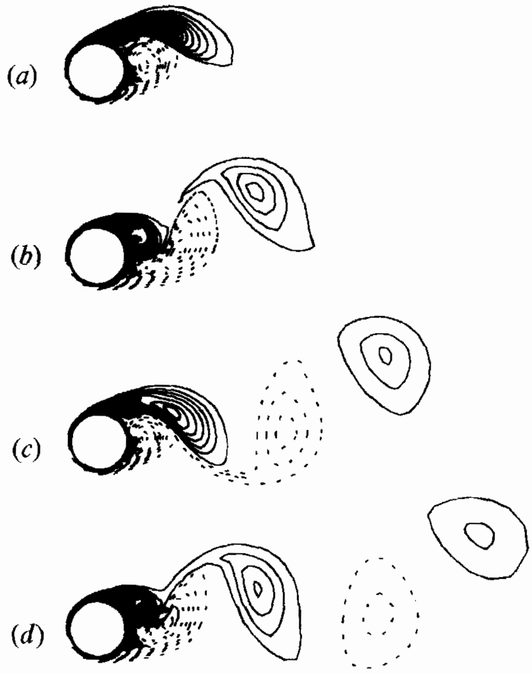

FIGURE 6. Vorticity contours at several time instants during two cycles of vortex shedding for $\alpha = 0.5$. (*a*) $t = 8$, (*b*) $t = 12$, (*c*) $t = 17$, (*d*) $t = 21$.

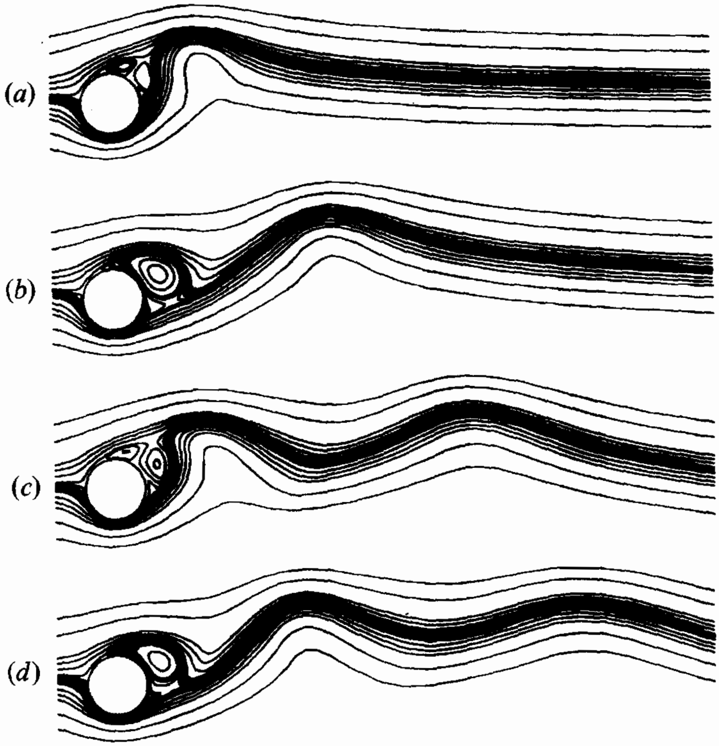

FIGURE 7. Patterns of instantaneous streamlines during two cycles of vortex shedding for $\alpha = 1$. (*a*) $t = 7$, (*b*) $t = 12$, (*c*) $t = 17$, (*d*) $t = 21$.

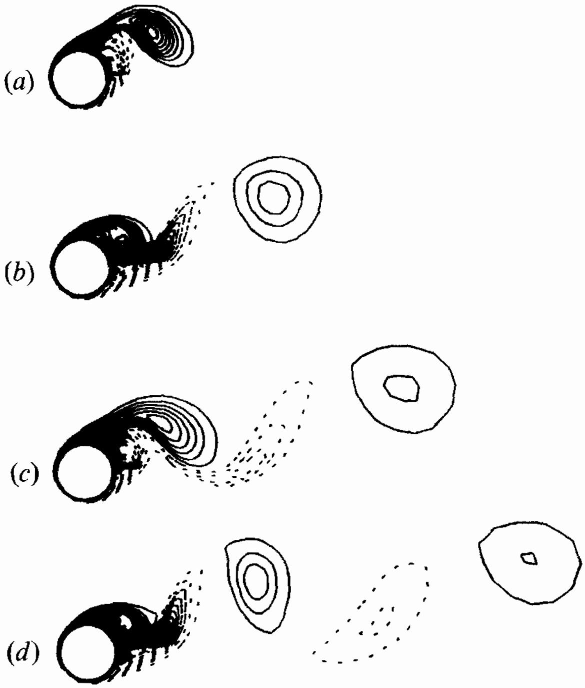

FIGURE 8. Vorticity contours at several time instants during two cycles of vortex shedding for $\alpha = 1$. (*a*) $t = 7$, (*b*) $t = 12$, (*c*) $t = 17$, (*d*) $t = 21$.

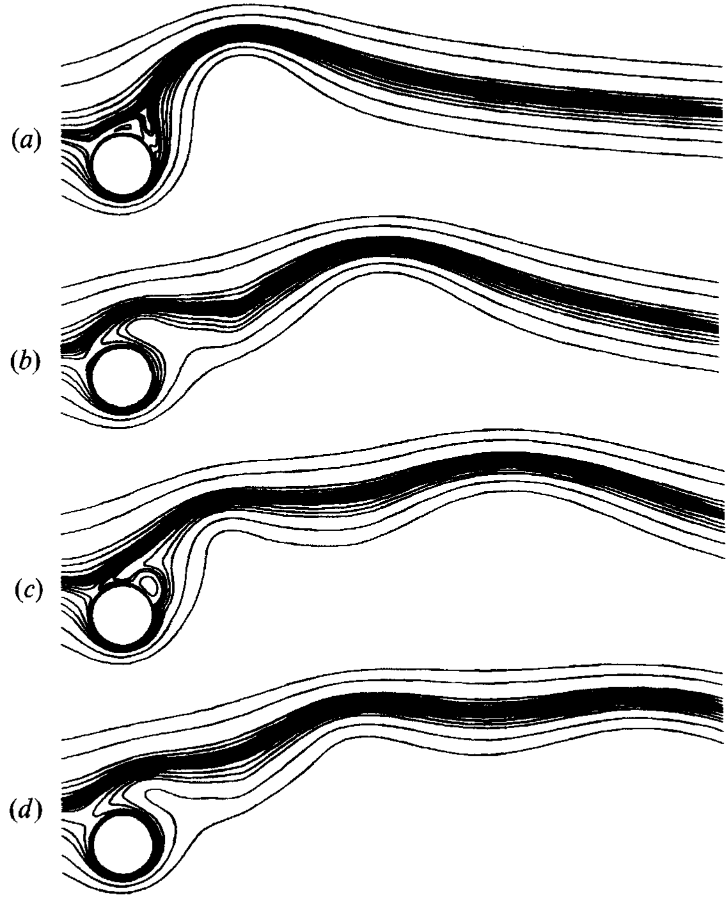

FIGURE 9. Patterns of instantaneous streamlines during two cycles of vortex shedding for $\alpha = 2$. (a) $t = 10$, (b) $t = 15$, (c) $t = 20$, (d) $t = 25$.

this difference in vorticity strength decreases with increasing time. This is expected since the net vorticity shed must be equal and opposite to the circulation around the circular cylinder induced by its rotation in order to satisfy Kelvin's circulation theorem. The net circulation around the cylinder is positive and thus the clockwise negative vortex shed from the upper side is stronger than the anticlockwise positive vortex shed from the lower side of the cylinder in the starting flows for a limited time. As vorticity is generated at a solid wall, an alternative view is that the opposing motion between the moving wall and the fluid on the upper side generates much stronger negative vorticity than the positive vorticity from the lower side where the relative velocity between the wall and fluid is smaller in the starting flows for a limited time. Owing to viscous effects, the relative velocity decreases with increasing time so that the circulation shed into the wake approaches a balance during one cycle of vortex shedding. This process can be seen in figure 23(c) from the time histories of lift and drag coefficients which are related to alternate vortex shedding. The lift amplitude associated with the first pair of vortices is much larger than for subsequent pairs which become uniform as time increases.

Figure 9 shows the pattern of instantaneous streamlines over two cycles of vortex shedding for $\alpha = 2$. For potential flow, the limiting case occurs at $\alpha = 2$ when the front and back stagnation points coincide. Any further increase in α will result in the lifting

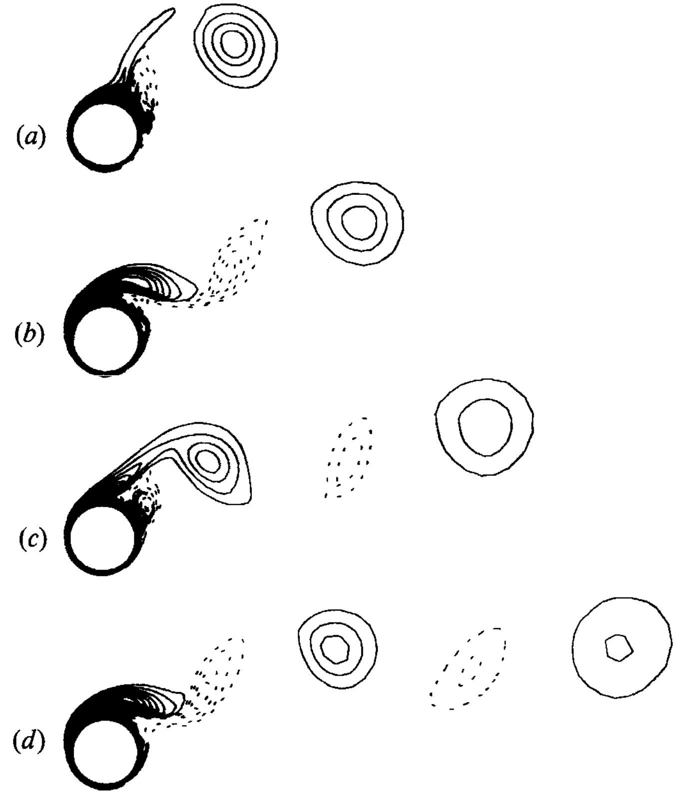

FIGURE 10. Vorticity contours at several time instants during two cycles of vortex shedding for $\alpha = 2$. (a) $t = 10$, (b) $t = 15$, (c) $t = 20$, (d) $t = 25$.

of the dividing or closed streamline and stagnation point away from the cylinder's surface. For viscous flow, the present study also found that when the peripheral speed of a rotating cylinder is greater than the maximum velocity around the cylinder induced by free-stream flow, the effect of rotation of the cylinder is much more dominant. When the first vortex is shed, the fluctuation of streamlines is relatively greater than when $\alpha = 0.5$ and 1. After a period of transient evolution, the fluctuation of the wavy streamlines decreases. Similar to the $\alpha = 0.5$ and 1 cases discussed earlier, the shedding of vortices from the two shear layers appears to be regular and alternate. However, the time taken for the first vortex to be shed is longer than when $\alpha \leqslant 1$, and the average shedding frequency is estimated to be 0.122 and the corresponding Strouhal number 0.244. Furthermore, the streamlines at the back of the cylinder are substantially deflected upward; and this feature continues progressively to a certain extent as time increases. It is observed that there are closed streamlines circulating around the rotating cylinder which divide the flow into inner and outer regions. In real flows this will lead to the formation of three-dimensional Taylor vortices (which is not simulated in the present two-dimensional study) in the inner region where the centrifugal effect is important (Matsui 1982). Although the wake is biased to the upper side in the near-wake region the streamline pattern is similar to that when $\alpha < 2$ in the far-wake region.

Figure 10 shows the vorticity contours at different time over two cycles of vortex shedding when $\alpha = 2$. As in figure 8, there is a difference in vorticity strength between the vortices shed from the upper and lower sides of the cylinder in starting flow only for a limited time. It is quite clear that the increase in α tends to suppress the process of positive vortex formation behind the cylinder. The present results are in good agreement with the numerical results of Badr *et al.* (1990). As α becomes larger, the meandering in the wake becomes smaller in amplitude and the frequency of vortices shed from the cylinder becomes larger.

Patterns of instantaneous streamlines for $\alpha = 3$ at different times are shown in figures 11 and 12. Figure 11 compares the evolution of the initial vortex structure of the present study and Badr *et al.* (1990) for the same Reynolds number $Re = 1000$. At $t = 1$, no vortices can be detected. At $t = 2$, a negative vortex is formed at the top of the cylinder and another negative vortex is formed in the region $90° < \theta < 180°$ after $t = 3$. These two vortices move in different directions, and as time increases one of the vortices is shed downstream, while the other migrates to the front part of the cylinder and disappears. This phenomenon has also been observed experimentally by Badr *et al.* (1990) which therefore supports the present computed results. For $\alpha = 3$, the flow pattern of wavy streamlines of periodic fluctuation observed for $\alpha \leqslant 2$ ceases to develop.

The time taken for the first vortex to be shed is larger than that for $\alpha \leqslant 2$. It can be seen in figures 12(*a*) and 12(*b*) that the attached vortex grows slowly until it becomes almost as large as the cylinder, before it is finally swept into the wake region by the free stream, as was also observed by Badr *et al.* (1990). The region of closed streamlines shown in figure 12 is much larger than when $\alpha = 2$. It is further noted from figure 12 that the flow field possesses only one stagnation point which is lifted away from the cylinder's surface. This phenomenon is similar to that reported by Badr *et al.* (1990), and the streamlines patterns are consistent with the flow patterns found experimentally in earlier studies by Prandtl & Tietjens (1934).

Figure 13 shows the pattern of instantaneous vorticity contours for $\alpha = 3$. It is interesting to note that in the present case a periodic flow pattern does not develop with time, and the positive vortex and the negative vortex are shed at the same time. In other words, the negative vorticity shed engulfs and neutralizes the positive vorticity. The vortex shedding process becomes totally different from that for $\alpha \leqslant 2$, and the vortices are only shed from the upper shear layer. As time increases, as predicted by Badr *et al.* (1990) the flow approaches a steady state. The present result differs from the case $\alpha > 2$ at $Re = 200$ studied by Chen *et al.* (1993). Their results show that shedding of more than one vortex occurs at $\alpha = 3.25$ and the shedding process is very different from that associated with the usual Kármán vortex street for $\alpha = 0$.

The present computation continues up to $\alpha = 6$ which has not been reported previously by other researchers. For $\alpha = 4$, the development of the flow structure with time is shown in figure 14. At $t = 1$, a negative vortex is formed in the region $0° < \theta < 90°$. At $t = 2$, this vortex moves into the region $90° < \theta < 180°$ and disappears shortly after. The appearance of two negative vortices simultaneously on the upper side of the cylinder as observed in figure 11(*d*) at $\alpha = 3$ does not occur in the present case. At $t = 3$, a second negative vortex is formed at the top of the cylinder, and as time increases, it grows and is then washed downstream. Patterns of streamlines should be compared with the case of $\alpha = 3$. It will be seen that the development of flow is similar to the case of $\alpha = 3$ after $t > 5$ except that the recirculating closed streamline region is larger and the stagnation point is lifted further away from the cylinder's surface.

Figure 15 shows a sequence of flow patterns for $\alpha = 6$. The flow shows similar behaviour to the case of $\alpha = 4$, except that no negative vortex appears in the region $90° < \theta < 180°$ at $t < 3$ as shown in figures 15(*a*) and 15(*b*). At $t = 3$, only one negative vortex is formed in the region $0° < \theta < 90°$.

(*a*) Present

(*b*) Present

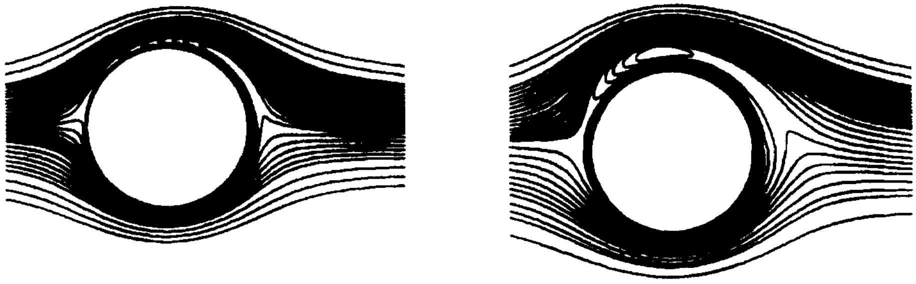

Badr *et al.* (1990)

Badr *et al.* (1990)

FIGURE 11(*a*,*b*). For caption see page 55.

It is found from the calculation that when α is larger than 2, alternate vortex shedding does not take place and the conventional Kármán vortex street disappears entirely. However, it should be emphasized that a starting negative vortex is being shed downstream when $\alpha \geqslant 3$ before a steady state is reached. This phenomenon is similar to the generation of starting vortex when a loaded airfoil moves impulsively in a stationary fluid. When the circulation is fully developed and remains constant around the airfoil, the shedding of the starting vortex ceases. Thus it can be inferred that the circulation around the present rotating cylinder must remain constant when the Kármán vortex street disappears and some form of self-similarity in flow structure, pressure and shear stress distributions should exist.

Figure 16 is a plot of the locus of the first vortex centre. The results show that the locus shifts upward and forward initially as α increases before being swept downstream by the free stream. It is in agreement with the experiments of Badr *et al.* (1990) in the near wake. In the far wake the locus of the first vortex centre is parallel to the free stream.

4.2. *Kármán vortex street behind a rotating cylinder*

The evolution of a Kármán vortex street behind a rotating circular cylinder with increasing α is an important aspect of the present study. Figure 17 shows the instantaneous streamlines viewed from a frame that is fixed with respect to the undisturbed fluid. The multitude of vortices in a regular alternating arrangement is clearly distinguishable when α is small. It is noted that the vortex pattern near the cylinder in figure 17(*a*) is very similar to that in figure 3(*a*), and the attached vortices in figure 2(*a*) are now masked by the velocity field in the near wake of the cylinder. On the other hand, in a frame translating with the cylinder the shed vortices are hidden in the oscillating wake as shown in figure 2(*a*) when compared to the case in figure 17(*a*)

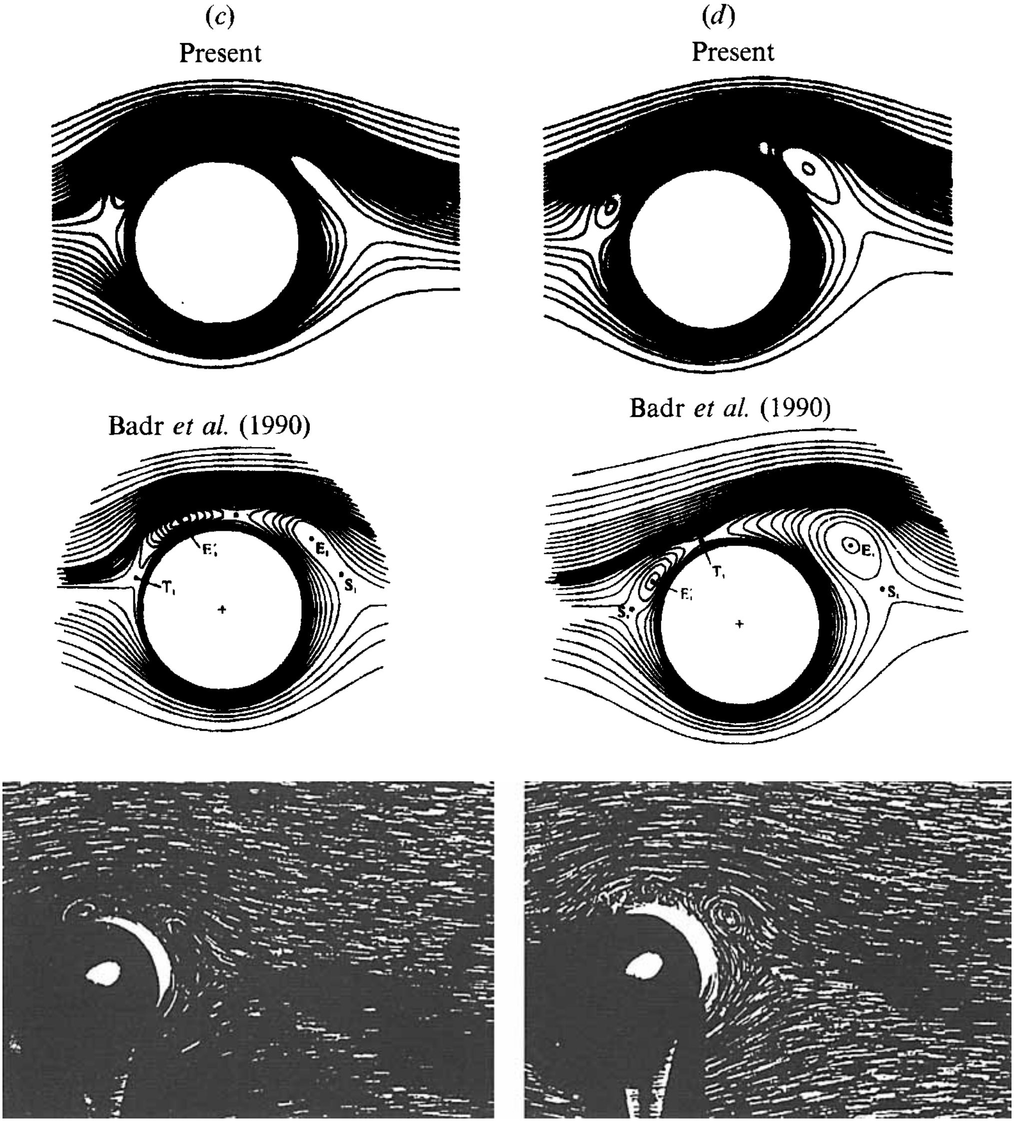
(*c*) Present

(*d*) Present

Badr *et al.* (1990)

Badr *et al.* (1990)

FIGURE 11(*c*,*d*). For caption see facing page.

for the same value of *t*. Since an attached vortex translates with the cylinder, it can be clearly observed in a frame translating with the cylinder (Chen *et al.* 1993). However, after the vortex is shed into the fluid, its core, especially in the far wake, is essentially stationary with respect to the undisturbed fluid although it actually moves very slightly in the direction of the cylinder translation resulting in the wavy streamline pattern of the wake as observed in figure 2. Therefore, it is generally easier to observe shed vortices in a frame that is fixed with respect to the undisturbed fluid.

The effects of the rotation in altering the vortex shedding seem to be as follows. When $\alpha = 0$, the terminology 'street' refers to the multitude of vortices in a regular alternating arrangement. The streamwise spacing of the vortices remains approximately constant and the cross-stream spacing increases in the streamwise direction. The ratio of cross-stream to streamwise vortex spacing increase slowly with distance in the wake, (*e*) (*f*)

Present Present

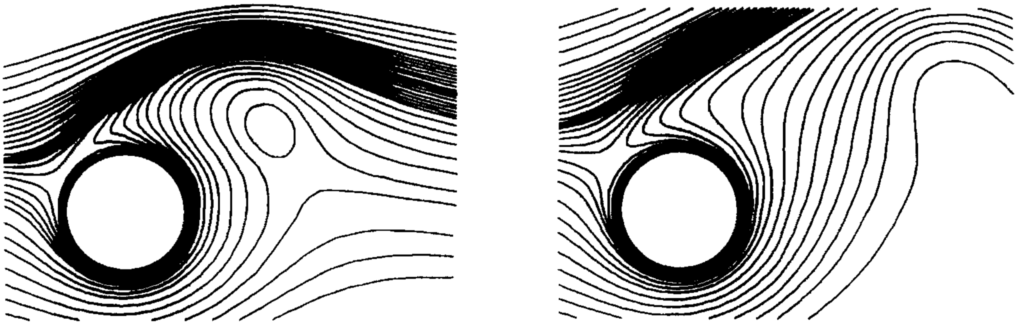

Badr *et al.* (1990) Badr *et al.* (1990)

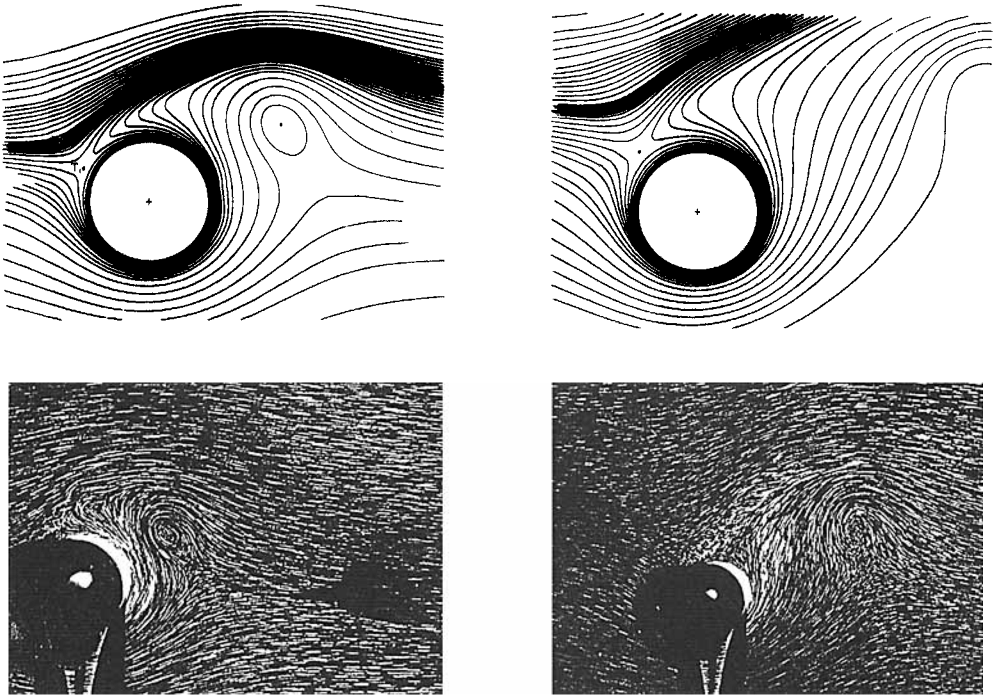

FIGURE 11. Comparison of the development of streamline patterns from two numerical methods and experimental flow visualization for $\alpha = 3$ at times (*a*) $t = 1$, (*b*) $t = 2$, (*c*) $t = 3$, (*d*) $t = 4$, (*e*) $t = 6$, (*f*) $t = 10$.

but this may be partially caused by the vortex diffusion of the grid numerical calculation. It is found that the region of constant positive streamlines around the cylinder decreases progressively when α increases and the region disappears completely when α is sufficiently high. When $\alpha \leqslant 2$, periodic vortex shedding remains and forms the Kármán vortex in the wake as shown in figure 17(*a–c*). When $\alpha \geqslant 3$, there are no regular vortices in the wake. The exact behaviour is sensitive to the value of α in the region $2 < \alpha < 3$ and so it is difficult to obtain a critical value of α at which the Kármán vortex street completely disappears. One can, however, find that the Kármán vortex street structure begins to deteriorate as soon as the peripheral velocity becomes greater

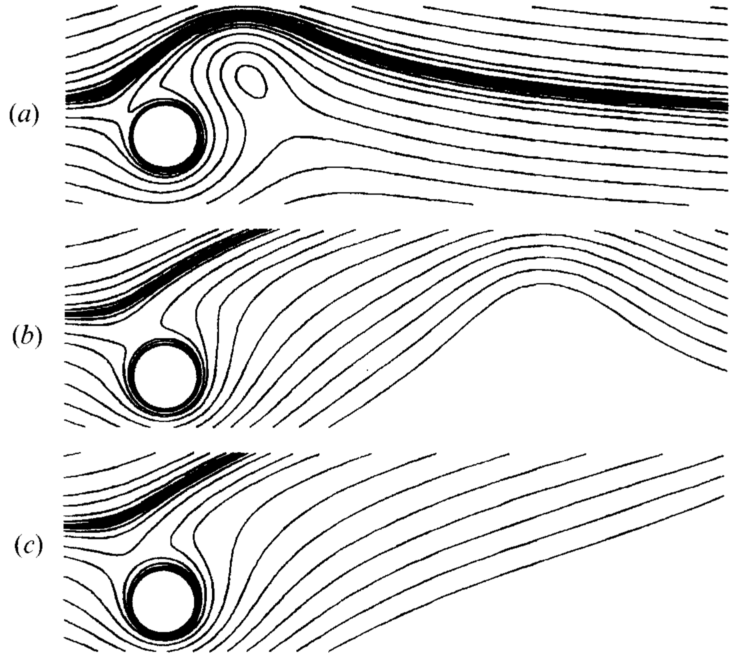

FIGURE 12. Patterns of instantaneous streamlines for $\alpha = 3$. (a) $t = 8$, (b) $t = 20$, (c) $t = 50$.

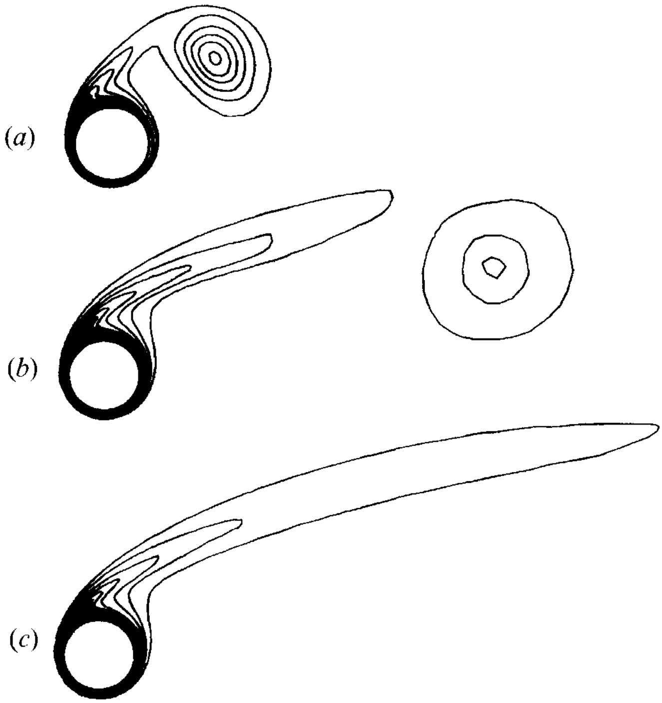

FIGURE 13. Vorticity contours at several time instants for $\alpha = 3$ at times (a) $t = 10$, (b) $t = 20$, (c) $t = 50$.

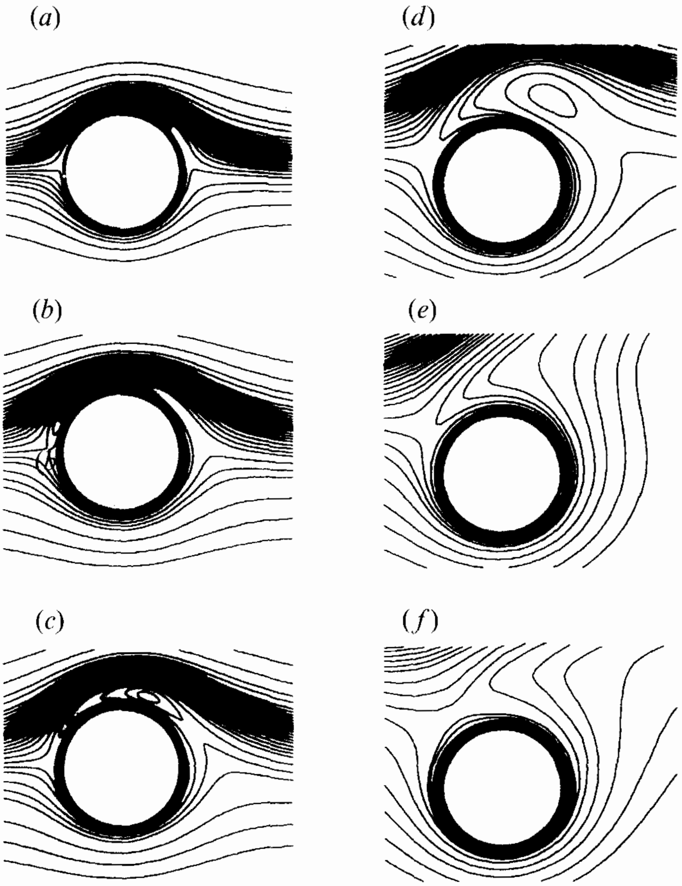

FIGURE 14. Patterns of instantaneous streamlines for $\alpha = 4$. (*a*) $t = 1$, (*b*) $t = 2$, (*c*) $t = 3$, (*d*) $t = 5$, (*e*) $t = 10$, (*f*) $t = 20$.

than the maximum velocity on the cylinder induced by the free-stream velocity (i.e. $\alpha \approx 2$) and finally disappears for $\alpha \geqslant 3$.

4.3. *Detailed features of the flow field*

A characteristic feature of flow around a circular cylinder that simultaneously rotates and translates in a stationary fluid is the asymmetric form of the velocity profiles, which vary according to the magnitude of α. To demonstrate the validity of the present numerical results some of them for initial velocity profiles are compared with the experimental and numerical results of Badr *et al.* (1990) at $\alpha = 0.5$. The present results as shown in figure 18(*a*) for radial velocity at $\theta = 0°$ are in better agreement with Badr's experimental data than their own computed results. They also indicate quantitatively the growth in attached vortices with increasing t and the approaching of velocity towards the free-stream value with increasing r. The radial and tangential velocity at $\theta = 90°$ in figure 18(*b*, *c*) indicate that the strong shear region caused by the cylinder's rotation is limited to about 20% of the radial distance from the wall.

Detailed velocity profiles around a rotating circular cylinder for $\alpha = 1$ at the instants when a negative vortex is shed and when a positive vortex is shed are shown in figures 19(*a*) and 19(*b*). For $\alpha = 6$, when vortex shedding ceases the velocity profile at $t = 20$

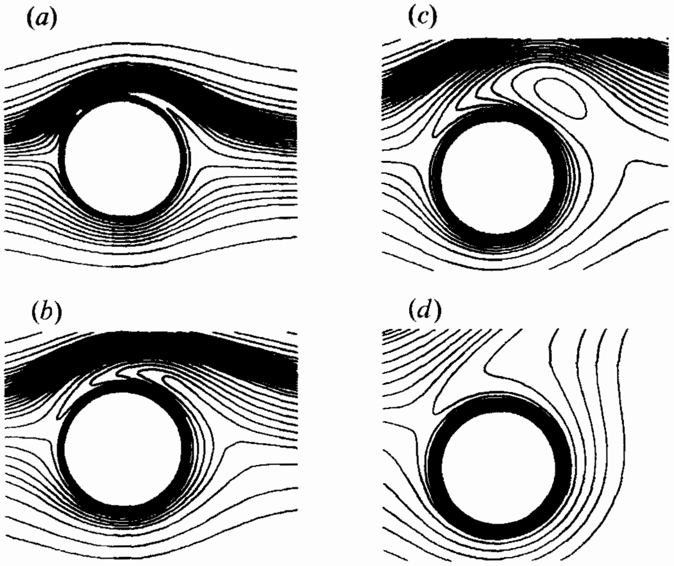

FIGURE 15. Patterns of instantaneous streamlines for $\alpha = 6$, (*a*) $t = 1$, (*b*) $t = 3$, (*c*) $t = 5$, (*d*) $t = 10$.

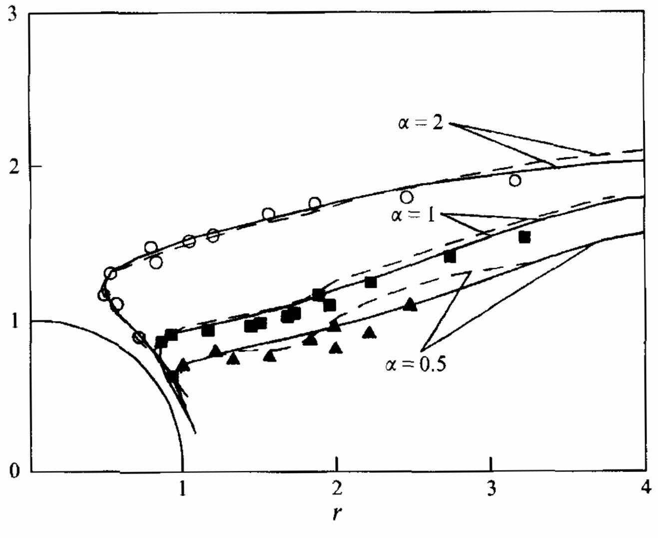

FIGURE 16. Comparison of computational and experimental results for the paths of the first vortex. ——, Present calculation; ---, Badr *et al.* (1990)'s calculation; Badr *et al.* (1990)'s experiment: ▲, $\alpha = 0.5$; ■, $\alpha = 1$; ○, $\alpha = 2$.

is shown in figure 19(*c*). When $\alpha \leqslant 1$, the overall velocity decreases and increases on the upper and the lower sides of the cylinder respectively because of the anticlockwise rotation of the cylinder. On the other hand, the velocities of the fluid relative to the wall increase with increasing α on the upper side of the cylinder whereas the opposite applies to the lower side. When α is sufficiently high, it is clearly seen from figure 19(*c*) that the fluid in a region near the surface is in enforced motion with the cylinder. As α increases the region becomes larger, and the relative velocities of the fluid near the

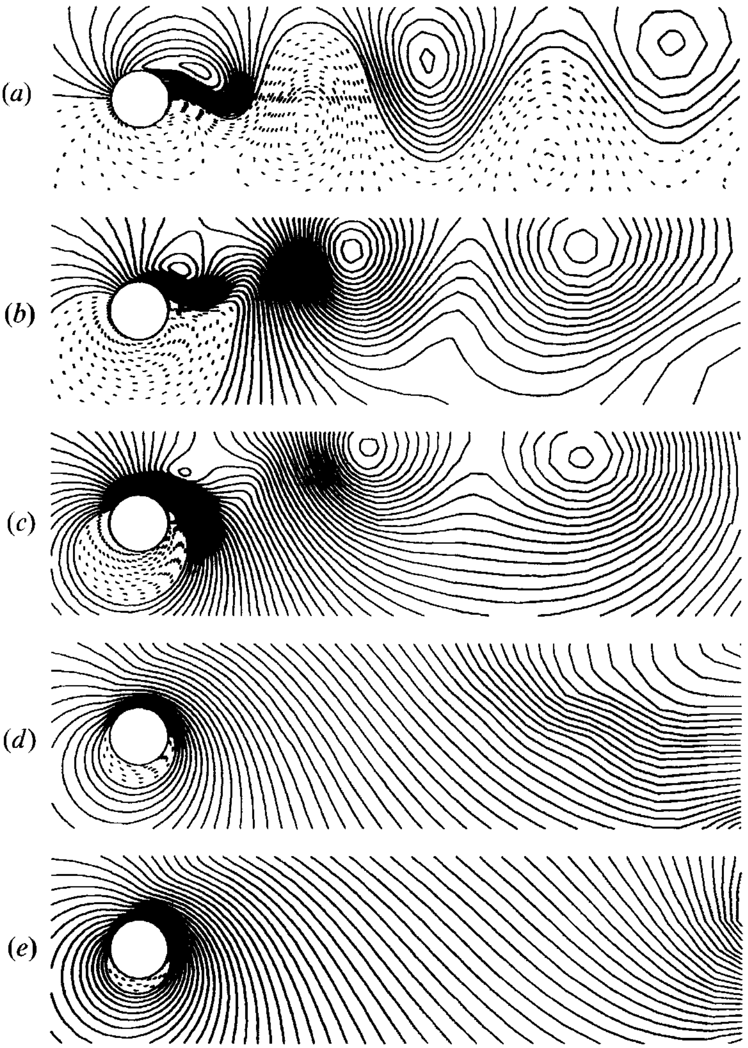

FIGURE 17. Instantaneous streamlines viewed from a frame fixed with the undisturbed fluid. (*a*) $\alpha = 0$, $t = 55$; (*b*) $\alpha = 1$, $t = 50$; (*c*) $\alpha = 2$, $t = 50$; (*d*) $\alpha = 3$, $t = 50$; (*e*) $\alpha = 4$, $t = 50$.

surface and the wall decrease with increasing α both on the upper and the lower sides of the cylinder.

It is of interest to locate the flow separation point and stagnation point. It is well known that the criterion of vanishing wall shear is not necessarily a meaningful indication of separation in the case of a moving wall. In the present study, separation points are determined by the MRS condition (i.e. $\partial v_\theta/\partial r = 0$, and $v_r = v_\theta = 0$) (Ludwig 1964; Inove 1981), and the stagnation point is determined by the condition $v_r = v_\theta = 0$. It can be seen from figures 19(*a*) and 19(*b*) that the separation points marked by small circle in the flow do not occur at the wall, but at a certain height above it. On the upper side of the cylinder, the wall moves upstream. The velocity changes sign from positive to negative along the r-direction at the separation point, and flow separation occurs at a position where there is a relatively large region of near zero velocity. However, on the lower side of the cylinder, the wall moves downstream. The velocity is of the same sign along the r-direction near the separation point, which differs from that on the upper

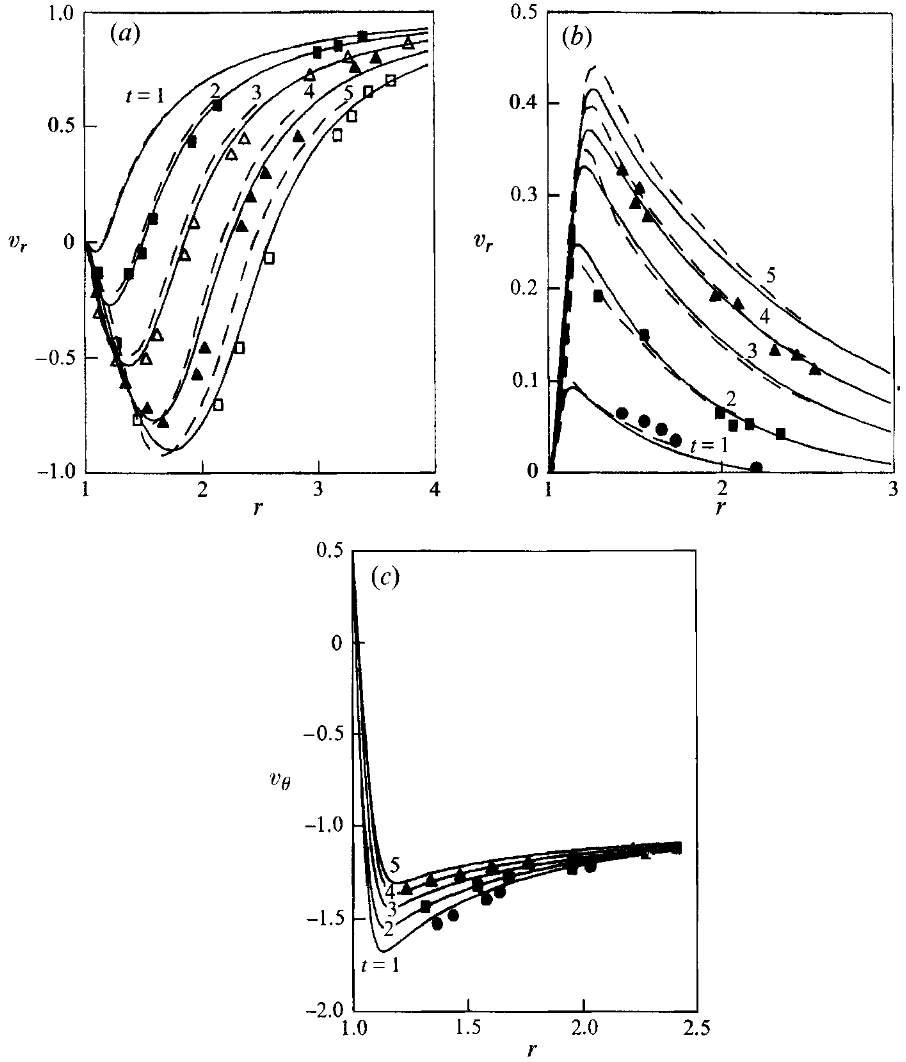

FIGURE 18. Comparison of velocity profiles for $\alpha = 0.5$. (a) v_r versus r at $\theta = 0°$, (b) v_r versus r at $\theta = 90°$, (c) v_θ versus r at $\theta = 90°$. ——, Present calculation; – – –, Badr *et al.* (1990)'s calculation. Experiment points taken from Badr *et al.* (1990): ●, $t = 1$; ■, $t = 2$; △, $t = 3$; ▲, $t = 4$; □, $t = 5$.

side. From calculation it is found that when $\alpha \leqslant 2$, there are two separation points. When $\alpha \geqslant 3$, no separation point can be detected but one stagnation point exists. As α increases, the stagnation point moves away from the cylinder along the radial direction.

The variations of mean positions of the front stagnation point and the separation points are plotted against α in figure 20. Here, the effects of rotation are clearly revealed. Both the separation points move along the anticlockwise direction of rotation with increasing α, with the rate of movement of the separation point on the lower side of cylinder being higher. In other words, the separation was delayed (moved downstream) when the wall moved in the direction of the flow and was advanced (moved upstream) when the wall moved opposite to the flow. The stagnation point however moves in the direction opposite to the rotation with increasing α. Its variation

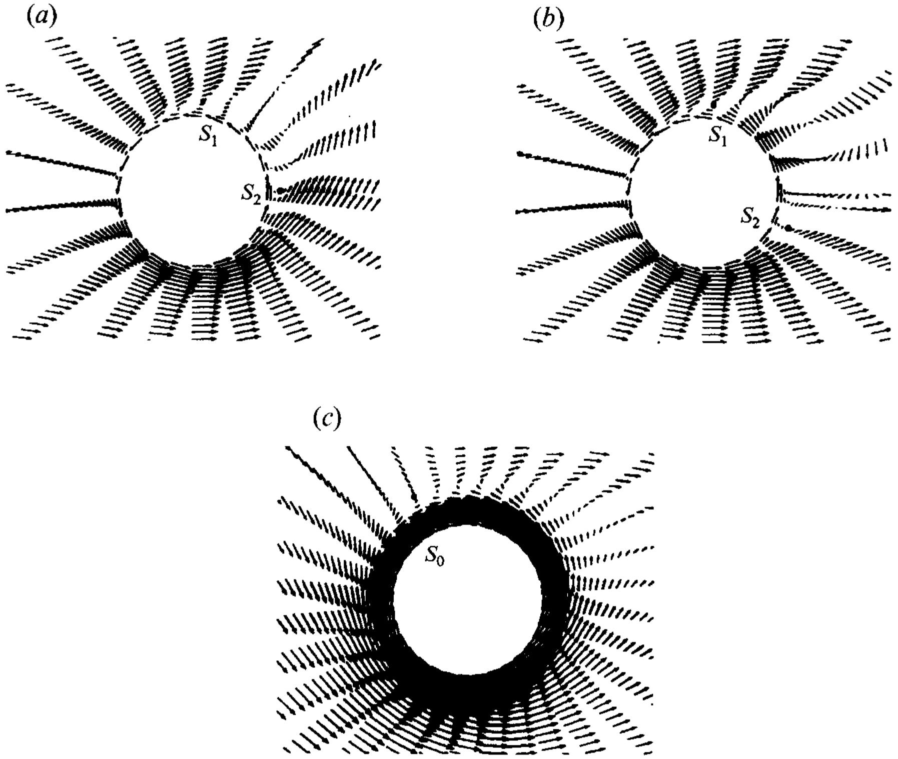

FIGURE 19. Velocity distribution around the cylinder. (*a*) and (*b*) $\alpha = 1$, $t = 7$ and $t = 12$ (during one cycle of vortex shedding); (*c*) $\alpha = 6$, $t = 20$.

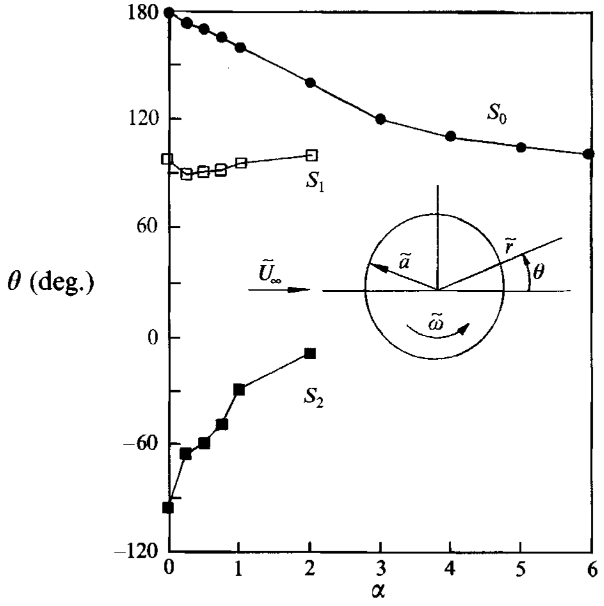

FIGURE 20. The variation of the stagnation point and the separation points with α. —●—, Stagnation point S_0;—⊟—, top separation point S_1; —■—, bottom separation point S_2.

with α taper off at high α as the flow structure become self-similar. The results agree with the experimental observations of Ludwig (1964) and Chew (1987).

For $\alpha \leqslant 2$, the wake region as demarcated by the two separation points decreases with increasing α. The narrowing of the wake, together with the shift of separation points and stagnation point leading to increased circulation around the cylinder with increasing α, seems to indicate that the rotation of circular cylinder can impart circulation to the fluid indefinitely within this range of α investigated. It must necessarily imply the increase in lift force with increasing α in accordance with Kutta–Joukowski's theorem.

4.4. *Surface pressure and friction drag distribution*

Figure 21 shows the variation of the calculated pressure coefficient C_p on the surface of the cylinder, which has not been computed by previous researchers. The dashed lines represent the instantaneous pressure distribution at different instances within a shedding cycle and the solid line represents the mean value over five cycles. Because vortices can be associated with a region of low pressure, their formation and subsequent shedding causes the pressure on the side of the cylinder to vary in a cyclic manner. This figure clearly indicates that as α increases, the pressure increases on the side of the cylinder where relative velocity is high and decreases on the other side of the cylinder, resulting in an increase in lift with increasing α.

For a stationary circular cylinder, the boundary layers separate after experiencing a region of adverse pressure gradient. However, the present study shows that even at as low as $\alpha = 0.5$, the adverse pressure gradient region on the upper half of the cylinder disappears and that on the lower half increases with increasing α. It also shows that the disappearance of, or increase in, the adverse pressure gradient region is not associated with a delay or early separation of the boundary layer as commonly found in the case of flow past a stationary cylinder. In a rotating cylinder, the wall is moving in the direction of the flow on the lower half of the cylinder. This imparts momentum to the boundary layer and delays separation even though it is subjected to a large adverse pressure gradient region. On the upper half of the cylinder, the opposing motion of the wall and fluid slows down the boundary layer and promotes early separation even though an adverse pressure gradient is absent. The underlying factor seems to be whether the imparting of momentum by the moving wall or dissipation of momentum by the adverse pressure gradient to the boundary layer is more dominant.

The minimum suction pressure on the lower half of the cylinder increases with increasing α and reaches -17.5 at $\alpha = 6$. Its position also shifts towards the rear of the cylinder as α increases beyond 0.5. At $\alpha \geqslant 2$, it is at $\beta \approx 240°$ ($\beta = 180° - \theta$) and constitutes a large increase in drag.

Another interesting feature to note is that the stagnation pressure coefficient reduces from 1 as α increases. At $\alpha = 2$ when a closed streamline circulating around the cylinder can be observed, it becomes less than zero. For $\alpha \geqslant 2$, the pressure coefficient is negative everywhere on the cylinder's surface and demonstrates the strong centrifugal effect caused by the cylinder rotation on the flow. There is a strong similarity between the pressure distribution curves at $\alpha \geqslant 3$ (figure 21*e*, *f*). The maximum and minimum pressure locations are at $\beta \approx 30°$ and 240° respectively and the range of C_p variation is about 6.5. The stronger centrifugal effect at $\alpha = 6$ than at $\alpha = 3$ merely shifts the entire pressure distribution towards the more negative direction by about 10 units. The results indicate that for $\alpha > 2$ when vortex shedding ceases and closed streamlines circulating around the cylinder are formed, the two-dimensional flow structure approaches some form of self-similarity (see streamline patterns at large t for $\alpha \geqslant 3$ in

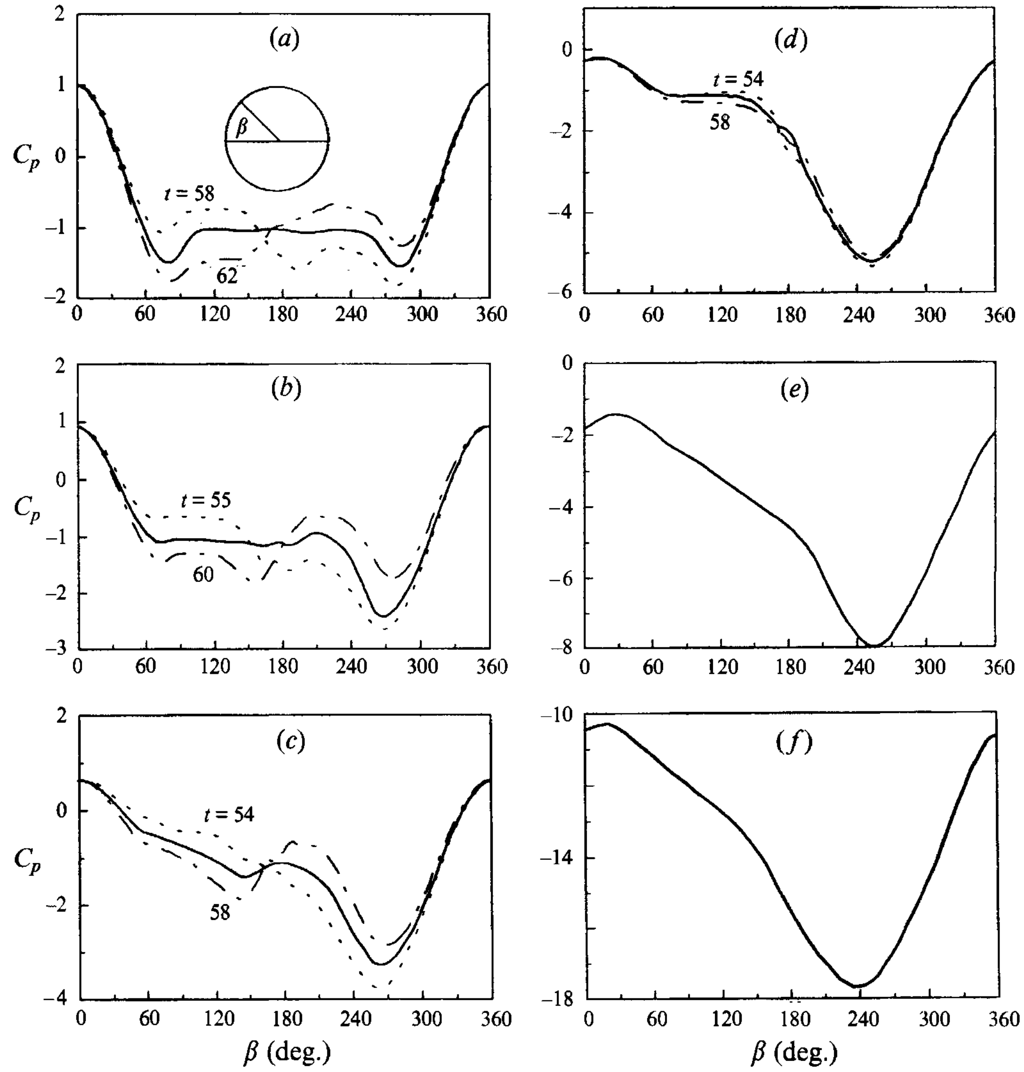

FIGURE 21. Pressure distribution on the surface of the cylinder (*a*) $\alpha = 0$; (*b*) $\alpha = 0.5$; (*c*) $\alpha = 1$; (*d*) $\alpha = 2$; (*e*) $\alpha = 3$; (*f*) $\alpha = 6$. ———, Positive vortex shedding; ---, negative vortex shedding; ——, mean value (over five cycles of vortex shedding for $\alpha \leqslant 2$).

figures 12, 14 and 15) which manifests itself as a similarity in pressure distribution. The similarity in pressure distribution will lead to asymptotic values of the mean lift and drag coefficients $\bar{C}_L$ and $\bar{C}_D$ at high α, which trend is discussed in §4.5.

Figure 22 shows the variation of the mean shear stress distribution of the surface of the cylinder at different α. The distribution is observed to be antisymmetric at $\alpha = 0$. At non-zero α, the magnitude of mean shear stress increases and decreases with increasing α on the upper and lower sides of the cylinder respectively which is consistent with the variation in relative velocity between the fluid and the cylinder. The approximately constant shear stress region in the wake of cylinder for $\alpha < 2$ can also be observed. The tendency towards similarity in shear stress at $\alpha = 3$, 4 and 6 also supports the previous argument that the flow structure approaches some form of self-similarity. Another point to note is the limiting value of mean shear stress at -0.12 at

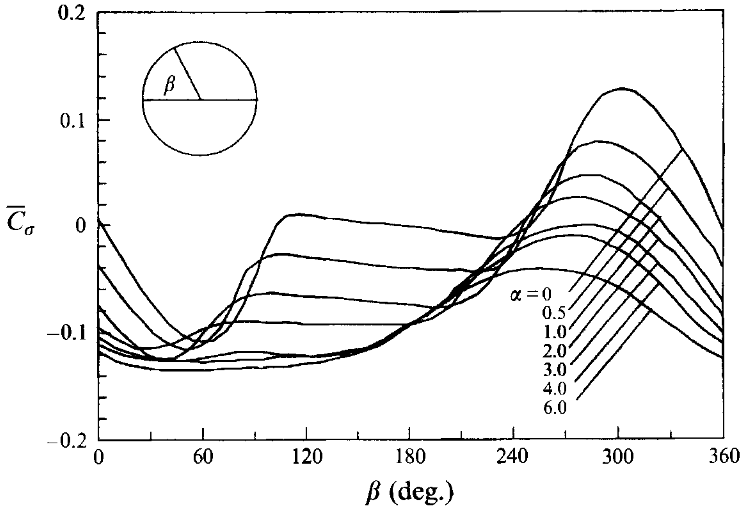

FIGURE 22. Mean shear stress distribution on the surface of the cylinder at different α.

high α. It seems that the growth in the recirculating region with α imposes a fixed velocity gradient at the wall even though the cylinder is rotating faster.

4.5. *The time histories of lift and drag coefficients*

One of the central problems for computational fluid dynamicists is to accurately predict aerodynamic loads. The time histories of total lift and drag coefficients C_L, C_D, their pressure components C_{Lp}, C_{Dp} and their friction components $C_{L\sigma}$, $C_{D\sigma}$ are shown in figure 23. When $\alpha = 0$, the mean fluctuation amplitude of the lift coefficient $\bar{C}_{Lmax}$ is 1.1, which is higher than the ≈ 0.8 reported by Ling, Ling & Wang (1992) and is in close agreement with the ≈ 1.05 reported by Tabata & Fujima (1991), both at the same Reynolds number. Stansby & Slaouti (1993) reported a value of $\bar{C}_{Lmax} \approx 0.3$ and 0.6 at $Re = 60$ and 180 respectively in their computation. The present result at $Re = 1000$ follows the correct trend that $\bar{C}_{Lmax}$ increases with increasing Reynolds number according to available computed results in the literature. Comparisons of the behaviour of the lift and drag at small and large α shows that when $\alpha \leqslant 1$, the lift and drag coefficients show regular fluctuations with a constant amplitude except during the starting (transient) stage of the flow. It is clear that the periodic fluctuation is related to alternate vortex shedding as shown in figure 23(*a*–*c*). In the range $1 < \alpha \leqslant 2$, the lift and drag signals are still periodic but begin to exhibit some high-frequency content as shown in figure 23(*d*). This means that an unstable transition occurs before vortex shedding ceases to occur at $\alpha > 2$. When $\alpha > 2$, the lift and drag signals become non-periodic and they are shown in figure 23(*e*).

It is interesting to note how the drag coefficient varies with α. When $\alpha = 0$, the drag coefficient fluctuates at twice the frequency of the lift coefficient as expected. As α increases, one of the peaks of the drag coefficient fluctuation clearly decreases and disappears completely when $\alpha = 1$ (figure 23*c*). At that stage the lift and drag forces fluctuate at the same frequency. The difference in amplitude of the drag coefficient is due to the difference in location of vortices in relation to the rear of the cylinder which also causes the mean lift coefficient to move away from zero.

When $\alpha < 1$, the higher the α, the shorter is the time required for the lift and drag forces to become periodic. When $\alpha > 1$, however, as longer time is required for

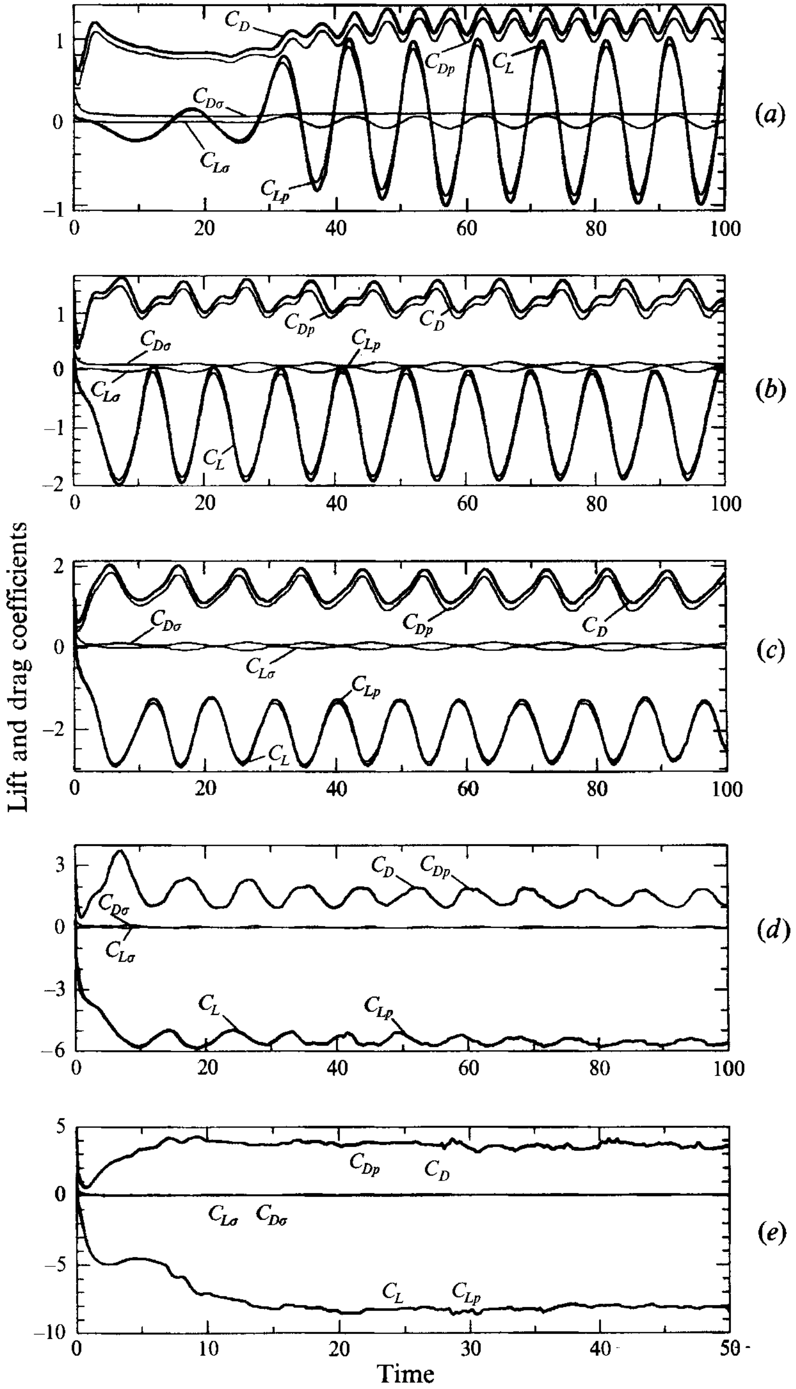

FIGURE 23. The variation of the lift and drag coefficients with α and time. (*a*) $\alpha = 0$; (*b*) $\alpha = 0.5$; (*c*) $\alpha = 1$; (*d*) $\alpha = 2$; (*e*) $\alpha = 4$.

periodicity to be established with increasing α, and a non-constant and generally damped amplitude of the forces is observed as in figure 23(*d*). It is also seen from figure 23 that the greatest contribution to the lift coefficient is given by the pressure forces: approximately 95% for $\alpha = 0$, 96% for $\alpha = 0.5$ and 99% for $\alpha = 3$. The shear stress contribution to the drag coefficient is also small.

4.6. *The global characteristics of the flow*

The shedding frequencies at various α are obtained from power spectra of the lift coefficients C_L (figure 24), and the variation of Strouhal number St with α is given in figure 25, where $St = 2\tilde{a}\tilde{f}/\tilde{U}_\infty$. It is clearly seen that the vortex shedding frequency, or Strouhal number St increases with increasing α up to $\alpha = 2$. At $\alpha = 3$, more than one peak is seen in the power spectrum with no particularly dominant frequency. This indicates that, for $\alpha > 2$, any vortex shed will be weak and the shedding is irregular.

The increase in Strouhal number with increasing α up to $\alpha = 2$ can be explained by the closer interaction between the two separated shear layers. It is evident in figure 20 that the two separation locations draw closer together with increasing α. The closer interaction of the two shear layers results in early roll-up and shedding of vortices. This is supported by the vorticity contours plots at different t and α in figures 3, 6, 8 and 10.

The mean values of the lift and drag coefficients, $\bar{C}_L$ and $\bar{C}_D$ respectively, and their ratio are shown in figure 26. When $\alpha = 0$, the estimated total mean drag coefficient, $\bar{C}_D$, is 1.14. This is in close agreement with the value of $\bar{C}_D \approx 1.1$ reported by some experimental researchers at the same Reynolds number. When $\alpha = 0.5$, 1, 2, 3, 4 and 6, the estimated total mean drag coefficients are 1.26, 1.36, 1.45, 2.8, 3.5 and 3.92 respectively. On the other hand, the estimated total mean lift coefficients at $\alpha = 0$, 0.5, 1, 2, 3, 4 and 6 are 0, -0.95, -2.38, -5.81, -7.82, -8.7 and -9.1 respectively. The lift coefficients determined by the present method are thus different from the results reported by Tokumaru & Dimotakis (1993) for $Re = 3.8 \times 10^3$ as the present coefficient never exceeds the limiting magnitude of 4π proposed by Prandtl (1925). The present results indicate the presence of asymptotic values of lift and drag coefficients at high α, consistent with earlier observations that the flow structure and pressure distribution tend towards self-similarity at $\alpha > 2$. The existence of a limiting $\bar{C}_L$ is proposed by Prandtl based on theoretical analysis, and implies that the Magnus effect is only effective up to a certain α. Higher lift can only be generated if there is an increase in negative vortices being shed downstream with increasing α. The existence of a dividing closed streamline around the rotating circular cylinder seems to prevent this from happening. However, in a real flow, three-dimensional effects are present and Görtler or Taylor vortices in the re-circulating region enclosed by the dividing closed streamline may alter the limiting $\bar{C}_L$ and $\bar{C}_D$ phenomenon observed in the present flow.

The lift coefficient increases at a faster rate than the drag coefficient as indicated by the lift to drag ratio which increases up to $\alpha = 2$. Beyond $\alpha = 2$, this ratio decreases slightly owing to the more rapid increase in drag. It seems that the optimum ratio (maximum in $|\bar{C}_L/\bar{C}_D|$) occurs at $\alpha \approx 2$ when a closed streamline circulating around the cylinder begins to appear. The appearance of a closed streamline at $\alpha = 2$ seems to form a demarcation line in the structure of the flow since beyond $\alpha = 2$, the periodicity in both the lift and drag forces disappears, and the drag force increases at a faster rate than the lift force.

Owing to viscous dissipation in the fluid, a moment about the axis of the cylinder is needed to do work in order to maintain its rotation. The relation between mean

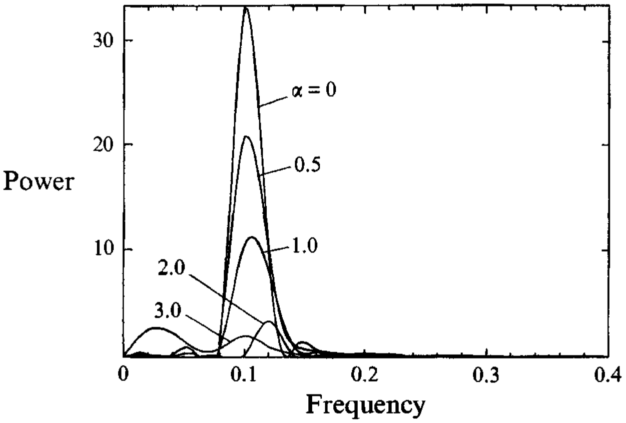

FIGURE 24. Power spectra of lift coefficients at different α.

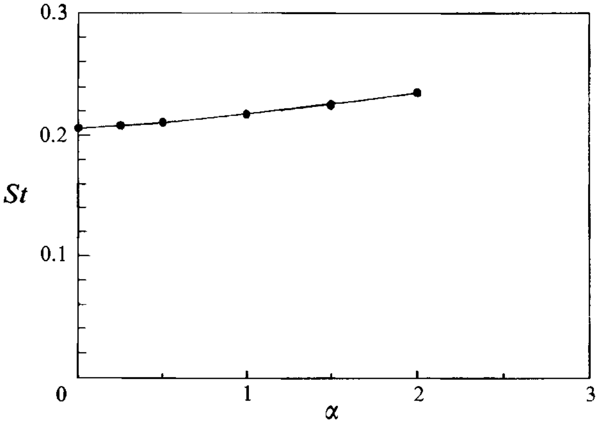

FIGURE 25. Variation of the Strouhal number St with α.

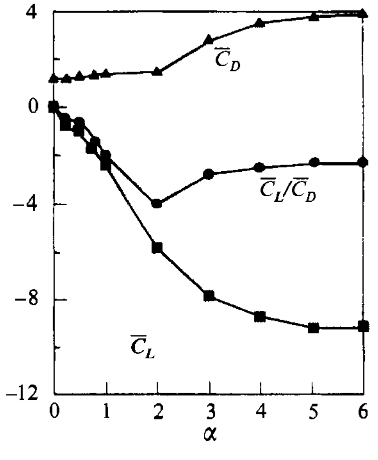

FIGURE 26. Variation of $\bar{C}_L$, $\bar{C}_D$ and $\bar{C}_L/\bar{C}_D$ with α.

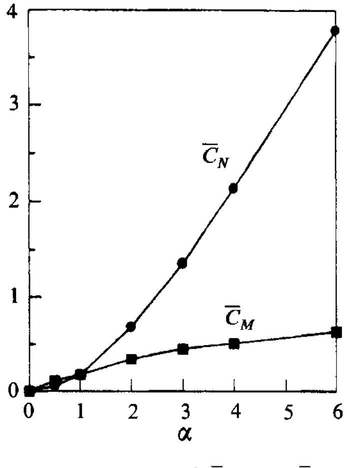

FIGURE 27. Variation of $\bar{C}_M$ and $\bar{C}_N$ with α.

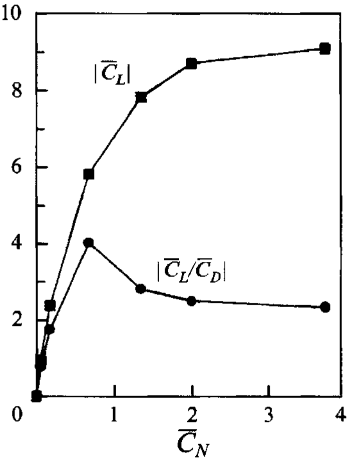

FIGURE 28. Variation of $|\bar{C}_L|$ and $|\bar{C}_L/\bar{C}_D|$ with $\bar{C}_N$.

moment and power coefficients $\bar{C}_M$ and $\bar{C}_N$ with α are shown in figure 27. The results show that the moment and power coefficients increase in magnitude with increasing α; but the variation of the moment coefficient appears to approach an asymptotic value with further increase of α which again is consistent with previous argument of self-similarity.

It is meaningful to plot $|\bar{C}_L|$ and $|\bar{C}_L/\bar{C}_D|$ against $\bar{C}_N$ in order to examine the economic feasibility of using the Magnus effect for lift generation. It is found from figure 28 that as $\bar{C}_N$ increases, there is at first a fairly rapid rise in $|\bar{C}_L/\bar{C}_D|$, but after a maximum is reached at $\bar{C}_N \approx 0.6$, $|\bar{C}_L/\bar{C}_D|$ decreases again and approaches an asymptotic value. Thus increasing power input beyond a certain level need not give rise to increasing lift force because of the presence of self-similarity in flow structure and pressure distribution. The usefulness of the Magnus effect in lift generation is thus limited.

5. Concluding remarks

The flow development past a rotating circular cylinder at $Re = 1000$ is investigated by a new hybrid vortex method. The present numerical computation confirms the flow features in the near wake for the initial stage obtained in experiments and numerical studies conducted by other researchers. In addition, the present work also provides some important information on the flow in the far wake over a long period of time and at larger α, which is virtually unreported in the literature. It is found that the vortex shedding and wake development behind the cylinder vary significantly dependent on the magnitude of the rotational parameter α. As α increases, the vortex street behind the cylinder in the near wake inclines as a whole towards the direction of rotation while the stagnation point moves opposite to the direction of rotation. The time required for the first vortex to be shed decreases with increasing α when $\alpha < 1$, and increases with increasing α when $\alpha > 1$. However, the fluctuation created by alternate vortex shedding becomes weaker in the far wake. As time advances the secondary vortex appears periodically. At $\alpha = 0.5$ and 1, it appears as a clockwise vortex on the lower side of the cylinder. However, at $\alpha = 3$, this secondary clockwise vortex only appears during the initial stage of flow on the upper side of the cylinder and migrates to the front part of the cylinder and disappears as time progresses. The Kármán vortex street structure begins to deteriorate as soon as the peripheral velocity becomes greater than twice the free-stream velocity and finally disappears for $\alpha > 3$.

The results predict a nearly linear variation of mean lift coefficient at low α, but it tapers off towards an asymptotic value at high α. Similarly, the dimensionless cylinder shedding frequency or Strouhal number increases with increasing α up to $\alpha = 2$. The present results seem to indicate the existence of a critical α at about 2 when a closed streamline circulating around the cylinder begins to appear. Below this critical α, Kármán vortex shedding exists, separation points can be found, the mean lift and drag coefficients and Strouhal number increase almost linearly with α. Above $\alpha \approx 2$, the region enclosed by the dividing closed streamline grows in size, vortex shedding ceases, the flow structure, pressure and shear stress distributions around the cylinder tend towards self-similarity with increasing α, and lift and drag coefficients approach asymptotic values. The optimum lift to drag ratio (i.e. maximum in $|\bar{C}_L/\bar{C}_D|$) occurs at $\alpha \approx 2$. The present investigation confirms Prandtl's postulation of the presence of limiting lift force at high α, and thus the usefulness of Magnus effect in lift generation is limited.

The numerical results show that the present method is capable of satisfactorily predicting the flow characteristics in the vicinity of cylinder surface, such as flow separation, surface vorticity distribution and radial and tangential velocity variation, as well as the global flow features, such as periodic variations of the flow, lift and drag forces, vortex shedding and Strouhal number. When comparison is possible, the results of the present computations are found to be in good agreement with the experimental and numerical results obtained by other investigators. The present method can be used for numerical simulation of bluff body flow at much higher Reynolds number and may exhibit even greater merit in the case of three-dimensional calculations.

REFERENCES

Badr, H. M., Coutanceau, M., Dennis, S. C. R. & Ménard, C. 1990 Unsteady flow past a rotating circular cylinder at Reynolds number 10^3 and 10^4. *J. Fluid Mech.* **220**, 459–484.

Badr, H. M. & Dennis, S. C. R. 1985 Time-dependent viscous flow past an impulsively started rotating and translating circular cylinder. *J. Fluid Mech.* **158**, 447–488.

BADR, H. M., DENNIS, S. C. R. & YOUNG, P. J. S. 1989 Steady and unsteady flow past a rotating circular cylinder at low Reynolds numbers. *J. Comput. Fluid.* **17**, 579–609.

BAR-LEV, M. & YANG, H. T. 1975 Initial flow field over an impulsively started circular cylinder. *J. Fluid Mech.* **72**, 625–647.

BARTON, G. 1989 *Elements of Green's Functions and Propagation Potentials, Diffusion and Waves.* Clarendon.

BOISVERT, R. 1984 A fourth-order accurate fast direct method for the Helmholtz equation. In *Elliptic Problem Solvers II* (ed. G. Binkhoff & A. Schoenstadt), pp. 35–44. Academic.

CHANG, C. C. & CHERN, R. L. 1991*a* A numerical study of flow around an impulsively started circular cylinder by a deterministic vortex method. *J. Fluid Mech.* **233**, 243–263.

CHANG, C. C. & CHERN, R. L. 1991*b* Vortex shedding from an impulsively started rotating and translating circular cylinder. *J. Fluid Mech.* **233**, 265–298.

CHEN, Y. M., OU, Y. R. & PEARLSTEIN, A. J. 1993 Development of the wake behind a circular cylinder impulsively started into rotatory and rectilinear motion. *J. Fluid Mech.* **253**, 449–484.

CHENG, M., LING, G. P. & ZHUANG, Y. G. 1990 Numerical simulation of the separated flow around a rotating circular cylinder in a uniform stream. *J. Hydrodyn.* (in Chinese) **5**, 65–73.

CHEW, Y. T. 1987 Flow past a rotating cylinder. In *Proc. Intl Conf. on Fluid Mechanics, Beijing, China* (ed. Q. Shuqing), pp. 556–560. Beijing University Press.

CHEW, Y. T., CHENG, M. & LUO, S. C. 1993 Simulation of flow around a rotating cylinder by a diffusion vortex scheme. In *Proc. Third Intl Offshore and Polar Engineering Conf., Singapore* (ed. J. S. Chung, B. J. Natvig, B. M. Das & Y. C. Li), vol. 3, pp. 404–408. Colorado: Golden.

CHORIN, A. J. 1973 Numerical study of slightly viscous flow. *J. Fluid Mech.* **57**, 785–796.

CHRISTIANSEN, J. P. 1973 Numerical simulation of hydromechanics by the method of point vortices. *J. Comput. Phys.* **13**, 363–379.

COLLINIS, W. M. & DENNIS, S. C. R. 1973 Flow past an impulsively started circular cylinder. *J. Fluid Mech.* **60**, 105–127.

COUTANCEAU, M. & MÉNARD, C. 1985 Influence of rotation on the near-wake development behind an impulsively started circular cylinder. *J. Fluid Mech.* **158**, 399–446.

GAD-EL-HAK, M. & BUSHNELL, D. M. 1991 Separation control: Review. *Trans. ASME* J: *J. Fluid Engng* **113**, 5–30.

GLAUERT, M. B. 1957 The flow past a rapidly rotating circular cylinder. *Proc. R. Soc. Lond.* A **230**, 108–115.

INOVE, O. 1981 MRS criterion for flow separation over moving walls. *AIAA. J.* **19**, 1108–1111.

JORDAN, S. K. & FROMM, J. E. 1972 Oscillatory drag, lift and torque on a circular cylinder in a uniform flow. *Phys. Fluids* **15**, 371–376.

KIMURA, T. & TSUTAHARA, M. 1987 Flows about a rotating circular cylinder by the discrete-vortex method. *AIAA J.* **25**, 182–184.

LING, G. C., LING, G. P. & WANG, Y. P. 1992 Domain decomposition hybrid method for numerical simulation of bluff body flows – theoretical model and application. *Science in China* A **35**, 977–990.

LU, Z. Y. & ROSS, T. 1991 Diffusing-vortex numerical scheme for solving incompressible Navier–Stokes equations. *J. Comput. Phys.* **95**, 400–435.

LUDWIG, G. R. 1964 An experimental investigation of laminar separation from a moving wall. *AIAA Paper* 64–6.

LYNCH, R. E. & RICE, J. R. 1978 High accuracy finite difference approximations to solutions of elliptic partial differential equations. *Proc. Nat. Acad. Sci.* **75**, 2541–2544.

MATSUI, T. 1982 Flow visualisation studies of vortices. In *Survey in Fluid Mechanics* (ed. R. Narasimha & S. M. Deshpande), pp. 145–164. Macmillan.

MODI, V. J., DOBRIC, A. & YOKOMIZ, T. 1993 Effect of momentum injection on the flow dynamics of bluff bodies. In *Proc. Third Intl. Offshore and Polar Engineering Conf., Singapore* (ed. J. S. Chung, B. J. Natvig, B. M. Das & Y. C. Li), vol. 3, pp. 501–513. Colorado: Golden.

MOORE, D. W. 1957 The flow past a rapidly rotating circular cylinder in an infinite stream. *J. Fluid Mech.* **2**, 541–550.

PELLER, H. 1986 Thermofluiddynamic experiments with a heated and rotating circular cylinder in crossflow, Part 2.1: Boundary layer profiles and location of separation points. *Expts. Fluids* **4**, 223–231.

PRANDTL, L. 1925 The Magnus effect and windpowered ships. *Naturwissenschaften.* **13**, 93–108.

PRANDTL, L. & TIETJENS, O. G. 1934 *Applied Hydro- and Aeromechanics* (transl. J. P. Den Hartog 1957). Dover.

REID, E. G. 1924 Tests of rotating cylinders. *NACA Tech. Note* 209.

ROSHKO, A. 1954 On the development of turbulent wakes from vortex streets. *NACA Rep.* 1191.

SARPKAYA, T. 1989 Computational methods with vortices – the 1988 Freeman scholar lecture. *Trans. ASME* J: *J. Fluids Engng* **111**, 5–52.

SCHLICHTING, H. 1968 *Boundary Layer Theory*. McGraw-Hill.

STANSBY, P. K. & SLAOUTI, A. 1993 Simulation of vortex shedding including blockage by the random-vortex and other methods. *Intl. J. Num. Meth. Fluids* **17**, 1003–1013.

STANSBY, P. K. & SMITH, P. A. 1991 Viscous forces on a circular cylinder in orbital flow at low Keulegan–Carpenter numbers. *J. Fluid Mech.* **229**, 159–171.

SWANSON, W. M. 1961 The Magnus effect: A summary of investigation to date. *Trans. ASME* D: *J. Basic Engng.* **83**, 461–470.

TA PHUOC LOC 1980 Numerical analysis of unsteady secondary vortices generated by an impulsively started circular cylinder. *J. Fluid Mech.* **100**, 111–128.

TABATA, M. & FUJIMA, S. 1991 An upwind finite element scheme for high-Reynolds-number flows. *Intl J. Num. Meth. Fluids* **12**, 305–322.

TANG, T. & INGHAM, D. B. 1991 On steady flow past a rotating circular cylinder at Reynolds numbers 60 and 100. *Comput. Fluids* **9**, 217–230.

TENNANT, J. S. 1976 Rotating cylinder for circulation control and airfoil. *J. Hydronaut.* **10**, 102–106.

TOKUMARU, P. T. & DIMOTAKIS, P. E. 1993 The lift of a cylinder executing rotary motions in a uniform flow. *J. Fluid Mech.* **255**, 1–10.

WILLIAMSON, C. H. K. 1989 Oblique and parallel modes of vortex shedding in the wake of a circular cylinder at low Reynolds numbers. *J. Fluid Mech.* **206**, 579–627.

WOOD, W. W. 1957 Boundary layer whose streamlines are closed. *J. Fluid Mech.* **2**, 77–87.